AN ATOMIC LAYER DEPOSITION PASSIVATED SURFACE ACOUSTIC WAVE SENSOR FOR BACTERIAL BIOFILM GROWTH MONITORING

By

Young Wook Kim

Thesis submitted to the Faculty of the Graduate School of
the University of Maryland, College Park, in partial fulfillment of the requirements for
the degree of Master of Science 2011

Advisory Committee:

Professor Reza Ghodssi
Professor Agis A. Iliadis
Professor Pamela Abshire

ABSTRACT

Title of Document: AN ATOMIC LAYER DEPOSITION PASSIVATED SURFACE ACOUSTIC WAVE SENSOR FOR BACTERIAL BIOFILM GROWTH MONITORING

          Young Wook Kim, Master of Science, 2011

Directed By: Professor Reza Ghodssi
          Department of Electrical and Computer Engineering
          The Institute for Systems Research

This thesis reports for the first time the design, fabrication, and testing of a reusable Surface Acoustic Wave (SAW) sensor for biofilm growth monitoring. Bacterial biofilms cause severe infections, and are often difficult to remove without an invasive surgery. Thus, their detection at an early stage is critical for effective treatments. A highly sensitive SAW sensor for biofilm growth monitoring was fabricated by depositing a high quality zinc oxide (ZnO) piezoelectric thin film by pulsed laser deposition (PLD). The sensor was successfully passivated by aluminum oxide (Al_2O_3) using Atomic Layer Deposition (ALD) to prevent ZnO damage from long term media contact. The sensor was reusable over multiple biofilm formation experiments using the ALD Al_2O_3 passivation and an oxygen plasma biofilm cleaning method. The SAW sensor was studied with *Escherichia coli* biofilm growth in Lysogeny Broth (LB) and in 10% Fetal Bovine Serum (FBS) as a simulated an *in vivo* environment. A multiple MHz level resonant frequency shift measured at the output of the SAW sensor in both LB and 10% FBS corresponded to the natural biofilm growth progression. These repeatable *E. coli* biofilm growth monitoring results validate the novel application of a SAW sensor for future implantable biofilm sensing applications.

Dedication

To my wife "Ui Kyoung Park", daughter "Sue Kim", parents in South Korea for everything

Acknowledgements

First of all, I would like to thank the committee members Prof. Pamela Abshire, Prof. Agis A. Iliadis, and especially my advisor, Prof. Reza Ghodssi, who provided his guidance and support throughout this degree process.

The author would also like to thank the members of the MEMS Sensors and Actuators Lab (MSAL) for all of their help, advice, and useful discussion. I would especially thank my BioMEMS colleagues, Peter Dystra, Mariana Meyer, Nathan Siwak, and Mike Fan, who helped me design the project. I also extend thanks to my collaborators on this research, Prof. William Bentley and his graduate students in helping me with bacterial growth and discussions.

Finally, I would like to thank the staff of the Maryland Nanocenter Fablab facility, Jonathan Hummel, John Abrahams, Tom Loughran and Jim O'Connor for their assistance with the tools used during the fabrication process.

Table of Contents

List of Tables

List of Figures

1. Introduction and Motivation

1.1 Bacterial Biofilm

Bacteria that attach to surfaces aggregate in a hydrated polymeric matrix of their own synthesis to form biofilms[1]. Biofilms constitute a protected mode of growth that allows survival in a hostile environment. The structures that form in biofilms contain channels in which nutrients can circulate, and cells in different regions of a biofilm exhibit different patterns of gene expression[2].
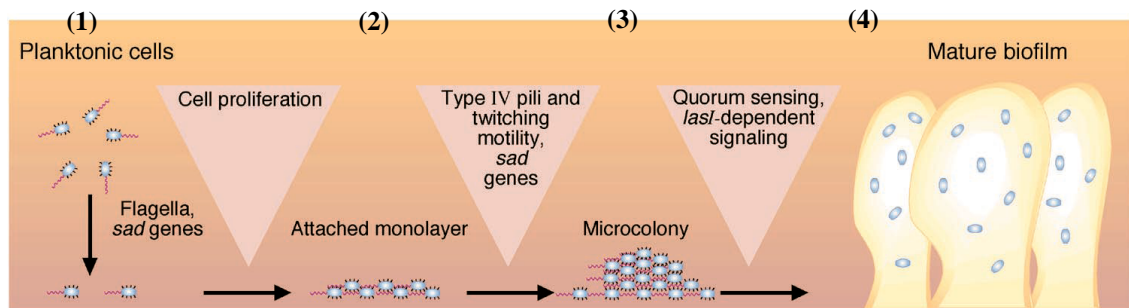
Figure 1.1: Schematic of the biofilm growth model[1] (1) Planktonic cells adhere on the surface, (2) Cell divide to form attached monolayer, (3) Formation microcolony, (4) Biofilm formation through quorum sensing

The schematic of the biofilm growth model is shown in Figure 1.1. A bacterial cell initiates the process of irreversible adhesion by binding to the surface using exopolysaccharide glycocalyx polymers. Cell division then produces sister cells that are bound within the glycocalyx matrix, initiating the development of adherent microcolonies. The eventual production of a continuous biofilm on the colonized

surface is a function of cell division within microcolonies and new recruitment of bacteria from the planktonic phase. Consequently, the biofilm finally consists of single cells and microcolonies of sister cells all embedded in a highly hydrated, predominantly anionic matrix of bacterial exopolymers and trapped extraneous macromolecules[3]. As the bacterial biofilm gradually occludes the colonized surface, newly recruited bacteria adhere to the biofilm itself. These bacterial biofilms are prevalent on most wet surfaces in nature and can cause environmental problems.

Biofilms growing in natural and industrial environments are resistant to bacteriophages and to the chemically diverse antibiotics used to combat biofilms in industrial processes[4]. As a result, the biofilms are much less susceptible to antibiotics than their nonattached individual planktonic counterparts. One mechanism of biofilm resistance to antimicrobial agents is the failure of an agent to penetrate the full depth of the biofilm. Polymeric substances like those that make up the matrix of a biofilm are known to retard the diffusion of antibiotics, and solutes in general diffuse at slower rates within biofilm than they do in water.

The relatively high levels of nutrients and the high surface area in many industrial aquatic systems, such as vessel and water purification systems, predispose these systems to biofilm formation. Adherent populations of bacterial biofilm bedevil most industrial systems by plugging filters and injection faces, fouling products, and generating harmful metabolic by-products, such as H_2S. For example, bacteria gradually colonize the water-cooled side of a metal surface in heat exchangers, and the resultant biofilm insulates against heat exchange so effectively that exchanger efficiency is gradually reduced to less than 10% of designed values. In addition,

bacterial corrosion of metals is an economically important consequence of bacterial biofilm formation that illustrates several fascinating aspects of the structure and physiology of these adherent bacterial populations[4].

Biofilms develop preferentially on inert surfaces, or on dead tissue, and on medical devices. Biofilms grow slowly, in one or more locations, and biofilm infections are often slow to produce overt symptoms. Sessile bacterial cells release antigens and stimulate the production of antibodies, but the antibodies are not effective in killing bacteria within the biofilm and may cause immune complex damage to surrounding tissue. Even in individuals with excellent cellular and humoral immune reactions, biofilm infections are rarely resolved by the host defense mechanism[5]. Antibiotic therapy typically reverses the symptom caused by planktonic cells released from the biofilm. Antibiotic treatments to biofilms can kill the majority of bacteria, and the number of truly resistant organisms within a biofilm typically is small. However, the minority of drug-resistant bacteria that persists after treatment tends to repopulate the biofilm. Furthermore, subsequent treatments of the repopulated biofilm only modestly reduce bacterial numbers, indicating that the repopulated biofilm is more resistant to the treatment. From a clinical perspective, these changes mean that traditional antibiotic therapy will never be successful against biofilm bacteria and that other modes of treatment will be needed to prevent biofilm formation in the first place. For this reason biofilm infections typically show recurring symptoms, after cycles of antibiotic therapy, until the sessile population is surgically removed from the body.

1.2 Bacterial Biofilms in Medical Implants

More than half a billion medical implants, such as heart valves, catheter and artificial hip joints shown in Figure 1.2, are performed every year in the United States[6, 7].
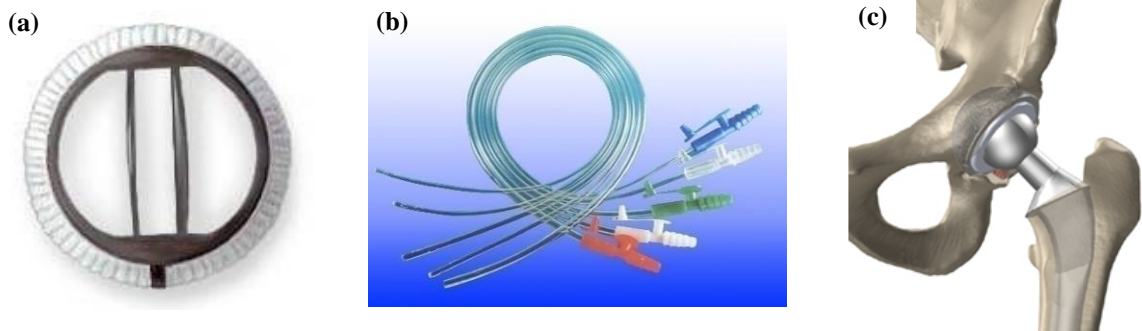
Figure.1.2: Examples of medical implants, (a) artificial heart valve (ADAM Inc.), (b) catheter (NSC Inc.), and (c) artificial hip joint (Zimmer Inc.)

Moreover, these numbers are expected to increase during the next decades because of an aging population with added risk factors. One of the side effects due to the medical implants is the infection from bacterial biofilm growth on implants. Biofilms in the artificial implants are not simply collections of individual bacteria. Instead, they are complex cooperative communities of microorganisms that contain one or more species embedded within an extracellular matrix. Biofilms can become a permanent feature of an infected device, meaning there may be no means to eradicate

the biofilm. Biofilms may also exhibit antibiotic resistance levels that are three or more orders of magnitude greater than those displayed by planktonic bacteria of the same strain[7, 8]. As a result, when a bacterial biofilm is formed, an invasive surgical procedure is often the most effective way to remove it. However, revisional surgery and care now cost in excess of $500,000 per patient[1,5].

Therefore, the continuous monitoring of biofilm formation in artificial implants is critical for early biofilm detection and treatment.

1.3 Bacterial Biofilm Detection Methods

1.3.1 Macro-scale Biofilm Detection Method

The most commonly used methods for pathogen detection involve traditional methods based on bacterial cell culture and colony counting,[9] and PCR based methods[10, 11]. Labeling with fluorescent molecules is also one of the well established techniques for bacterial detection. The procedure is not complicated, but the sensitivity is very high[12]. For instance, a fluorescent immunosensor for bacteria detection was demonstrated in Heyduk et al.[13] Two samples of the antibody were prepared, each labeled with nanometer-sized flexible linkers with short complementary oligonucleotides modified with fluorochromes that could participate in fluorescence resonance energy transfer (FRET) to increase the sensitivity. The schematic design is illustrated in Figure 1.3. These two

fluorescently labeled antibodies allowed for detection of even a moderate density

of bacteria.
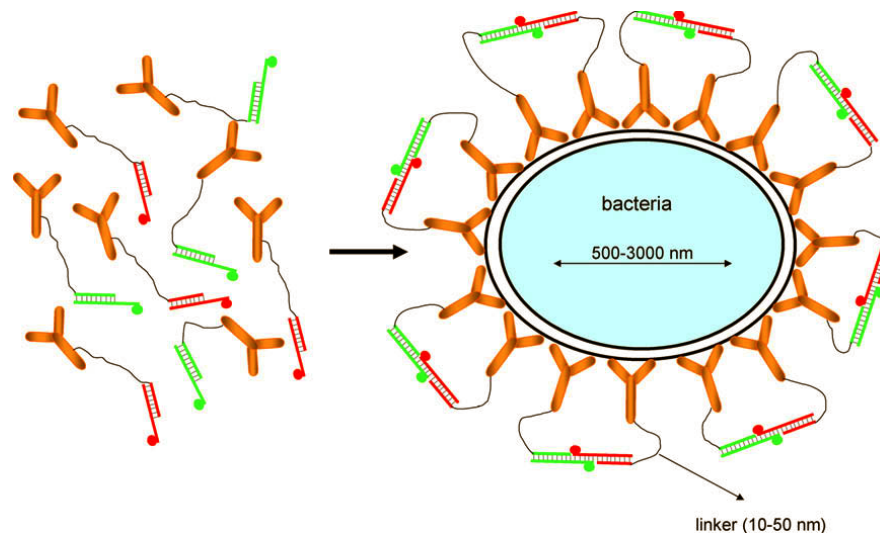
Figure 1.3: Design of homogeneous biological sensors for detecting pathogenic bacteria [13]

A fluorescent image showing the binding of the antibodies and bacteria is shown

in Figure 1.4.
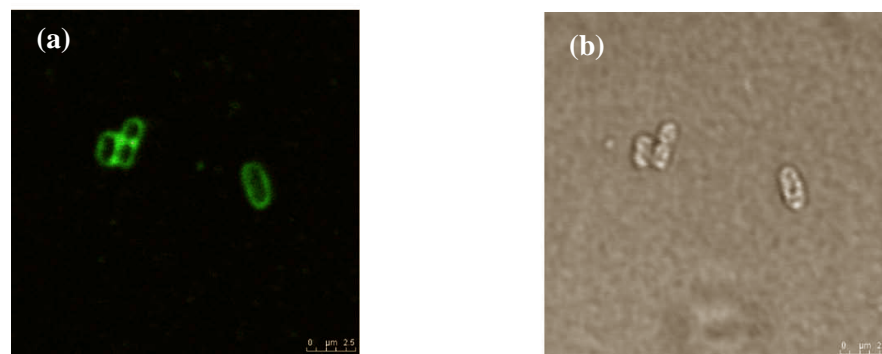
Figure 1.4: Fluorescence microscope image (a) fluorescent signal from the oligonucleotides proximity due to the bacteria binding, (b) light transmittance image in the same area [13]

As shown in Figure 1.4, this fluorescent method allowed for detection of a single cell. However, it required a fluorescent label on the probe molecule, and involved external equipments for the detection, which is not reasonable for implantable applications.

Another common method for bacterial detection is the Enzyme Linked Immunosorbent Assay (ELISA)[14]. ELISA is a specific and highly sensitive method for quantitative measurement of antibodies or analytes in solution as shown in Figure 1.5. ELISA has been used as a diagnostic tool in medicine as well as a quality check in various industries due to its high sensitivity [10].
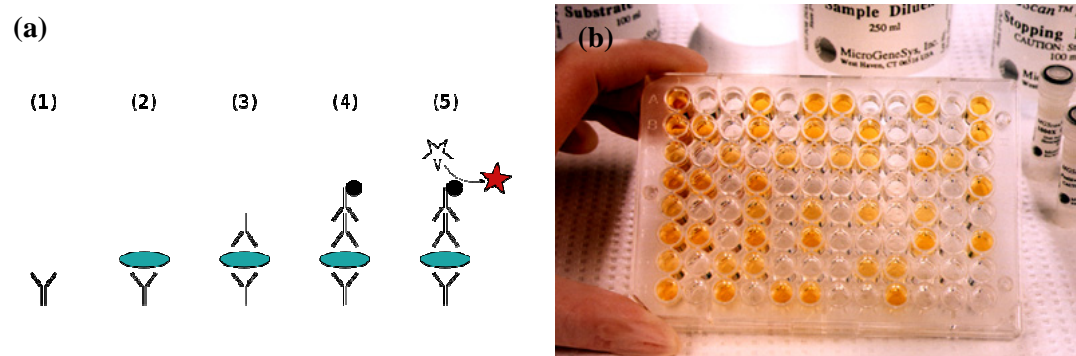
Figure 1.5: (a) Schematic of general ELISA procedure: (1) immobilize the probe antibody, (2) incubate sample, (3) incubate detection antibody, (4) incubate second conjugate antibody, (5) add fluorescent solution and read out, (b) ELISA 96 well plate [15]

In principle, an unknown amount of antigen is affixed to a surface in the ELISA plate, and then a specific antibody is applied over the surface so that it can

bind to the antigen. This antibody is linked to an enzyme, and in the final step a substance is added that the enzyme converts to a detectable signal, such as color change using a fluorescent molecule. In spite of the highly selective sensitivity of the ELISA, it is a slow procedure and challenging in lab-on-a-chip applications due to the multiple labeling requirements.

Electrochemical amperometric sensing is another common method for bacterial detection. Amperometric biosensors function by the production of a current when a static potential is applied between two electrodes. The major advantage of the amperometric biosensor is that the magnitude of the measured current is only due to the analyte of interest. Hence, if a specific antibody is immobilized on the sensor, it can achieve a highly selective electrical signal response only from the specific antigen. Since bacteria can generate electrons from their metabolism or interaction with the external environment, the amperometric electrochemical bacterial biosensor has been demonstrated by other groups[16, 17]. However, this method cannot be applied for an implantable sensor due to the long term static electric potential requirement, which can increase the total volume of the sensor due to battery needed to provide this potential.

These traditional methods offer reliability and selectivity, but are very time consuming and often requires external equipment.

1.3.2 Micro-scale Biofilm Detection Methods

Bacterial detection using microscale devices have been shown by many other groups. In J.M Song et al.[18], a CMOS biochip immunosensor was demonstrated for single bacterium detection. The sensor was functionalized based on the combination of ELISA and laser-induced fluorescence (LIF) detection. The schematic diagram of the biochip system is shown in Figure 1.6.

(a)

Antibody-immobilized capillary reactor

Diode Laser

Microscope Objective

Mirrors

Long Pass filter

CMOS-Based Biochip

(b)

Immobilized Antibody

Detector Antibody

Single Pathogenic Bacteria

Substrate

Cleaved Fluorescent from Substrate

Alkaline Phosphatase Labeled Antibody

Blocking agent

Amplification

AP
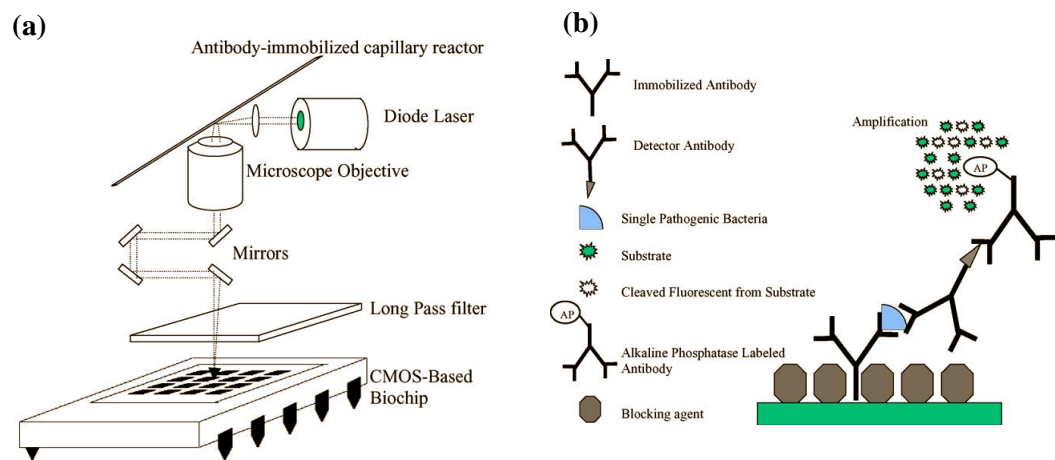
Figure 1.6: (a) Schematic diagram of the biochip system, (b) ELISA in the arrayed sensor: A lot of cleaved fluorescent were produced by enzymatic reaction between substrate and sandwich immunocomplex.

As shown in Figure 1.6(a), the diode laser beam was focused onto the detection window of an antibody immobilized capillary reactor using a lens. The laser beam was used to excite the enzymatic product, which had an emission at a specific wavelength when it was excited by the laser. For the specific bacterial reaction in each well, the wells were functionalized by the ELISA method as shown in Figure 1.6 (b). Using the multiarray biochip structure and specific

antibodies immobilization in the sensor, the output of the sensor was able to quantize the number of bacteria.

The impedance method was also used to detect a bacterial layer on the surface of microelectrodes in L. Yang et al [19]. The interdigitated electrodes were fabricated and bacteria were grown over the electrode in bacterial growth media. The impedance growth curves, impedance against bacterial growth time, were recorded during the growth of bacteria.

The ELISA-based microarray sensor and impedance method for the bacterial detection showed high detection limits (on the order of one cell), but they cannot be applied for *in vivo* bacterial sensing applications due to the requirement for external equipment, such as the laser for the ELISA based biosensor and battery for the impedance bacterial sensor.

1.3.3 Implantable Sensors

Developing an implantable biosensor for continuous monitoring *in vivo* of a pathogen has been one of the key challenges for researchers due to the complexities of the implantable biosensor, such as the biocompatibility of the material, overcoming biofouling, and human body variations. Due to these challenges, a successful biosensor for *in vivo* bacterial detection has not been demonstrated.

One of the successful implantable sensors is a blood pressure sensor for continuous monitoring. In Peng Cong et al.[20], a wireless batteryless implantable blood pressure sensor was demonstrated as shown in the schematics in Figure 1.7.
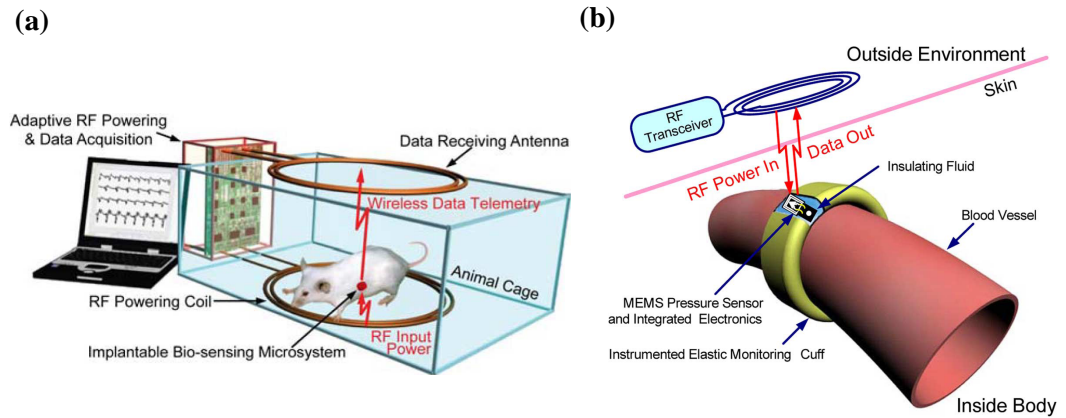
Figure 1.7: (a) *In vivo* real time wireless and batteryless biosensing microsystem. (RF inductive coupling was employed for the wireless communication), (b) Proposed implantable blood pressure monitoring microsystem (A biocompatible silicone elastic membrane was wrapped around a blood vessel, and a MEMS pressure sensor and electronics were implanted in the elastic band.)

As shown in Figure 1.7 (a) and (b), the pressure sensor was implanted in the biocompatible elastic band and the recorded blood pressure values were sent by the electronics and RF inductive coupling wireless communication to the external reader. However, this sensor cannot be fully implantable since the dimension of the sensor was too large to implant to human. Moreover, the elastic band around the vessel was not realistic for *in vivo* applications due to the requirement of invasive surgery.

2. Device Design

2.1 Design Considerations

The goal of this thesis work is developing a bacterial biofilm sensor for future implantable wireless bacterial sensing applications. The critical implantable application requirements should be considered at the design of the device.

First of all, the materials of the sensor have to be biocompatible so that they cannot be another infection source. The size of the device also should be small enough to be implanted in the body. One way to decrease the size of the device can be using a passive transduction mechanism which does not need a battery for operation. Finally, a high sensitivity of the sensor is required for reliability of the device in an *in vivo* environment.

Based on these requirements, the Surface Acoustic Wave (SAW) sensor[21,22] has many advantages for implantable applications. A SAW sensor can be fabricated using biocompatible materials, such as gold, zinc oxide (ZnO), and silicon[23]. Also the SAW sensor exhibits extremely high sensitivity. The detection limit of the SAW sensor has been shown up to an atto-gram (10^{-18}g),[24] which is one of the most sensitive detection methods. The SAW sensor is also a passive device, since the required power for the operation of the sensor can be delivered by RF inductive coupling[25, 26, 27] without a battery. Based on these advantages, the SAW sensor can be the optimal transduction method for implantable biofilm growth monitoring applications.

2.2   Surface Acoustic Wave Sensor

Since Rayleigh discovered the Surface Acoustic Wave (SAW) in 1887, SAW sensors have been used for diverse sensing applications.[28] A SAW is generated in the interdigitated transducer (IDT), which is on a patterned piezoelectric material, by applying an alternating current (AC) electrical signal. The IDT generates a uniform electric field on the surface of the piezoelectric material when a potential difference is applied between two electrodes, and it induces a uniform mechanical displacement based on the piezoelectricity of the material. Since the input electrical signal is an AC signal, a standing mechanical displacement wave in each IDT electrode pair is formed at the specific frequency. The standing wave is satisfied at the specific condition that the separation of the electrode pair is equal to an integer times half of the SAW wavelength[29], as shown in (1) and (2).

$$d = n\frac{\lambda}{2} \qquad (1)$$

$$v = f \cdot \lambda \qquad (2)$$

where d is the separation of the IDT electrode pair, λ is the wavelength of the SAW, n is an integer, v is the SAW speed, and f is the operational frequency. The speed of the SAW on the substrate is a given value in each different piezoelectric material[30, 31]. Based on these relations, we can design an operational frequency of the SAW by changing the pattern of the IDT or piezoelectric material.

The standing mechanical wave, which is induced by the electric field in the IDT on the piezoelectric material, propagates on the surface based on the reversible piezoelectricity of the substrate[32]. At first, the mechanical displacement induces the electrical field, and the induced electric field generates another mechanical displacement because of the reversible piezoelectric properties. These reversible energy conversions from mechanical to electrical energy occur sequentially on the piezoelectric substrate. As a result, the SAW propagates on the surface. The propagation of the SAW is governed by the three dimensional acoustic wave equation as shown in (3)[33].

$$\nabla^2 p - \frac{1}{v^2}\frac{\partial^2 p}{\partial t^2} = 0 \qquad (3)$$

where p is the acoustic pressure, ∇^2 is the Laplace operator, and v is the velocity of the SAW. If we assume the propagation area is constant, such as in the case of an isotropic material, the three dimensional acoustic wave equation can be simplified to the one dimensional acoustic wave equation, as shown in (4), and the velocity of the SAW is shown in equation (5)[34].

$$\frac{\partial^2 p}{\partial x^2} - \frac{1}{v^2}\frac{\partial^2 p}{\partial t^2} = 0 \qquad (4)$$

$$v = \sqrt{\frac{C}{\rho}} \qquad (5)$$

where x is the axis of the wave propagation, C is the shear modulus of the piezoelectric material, and ρ is the local density of the surface. Depending on the lattice structure of the substrate, two possible propagation modes of the SAW, which are called Rayleigh and Love modes, can be generated.

Lord Rayleigh discovered the vertical SAW mode of propagation and, in his classic paper, predicted the properties of these waves[35]. Named for their discoverer, Rayleigh waves have a longitudinal component and a vertical shear component as shown in Figure 2.1. The Rayleigh SAW amplitude is typically about 10 Å and the wavelength ranges from 1 to 100 μm. This type of SAW sensor usually operates from 25 to 500 MHz[36].

Vertical and Shear Component

Propagation of the SAW
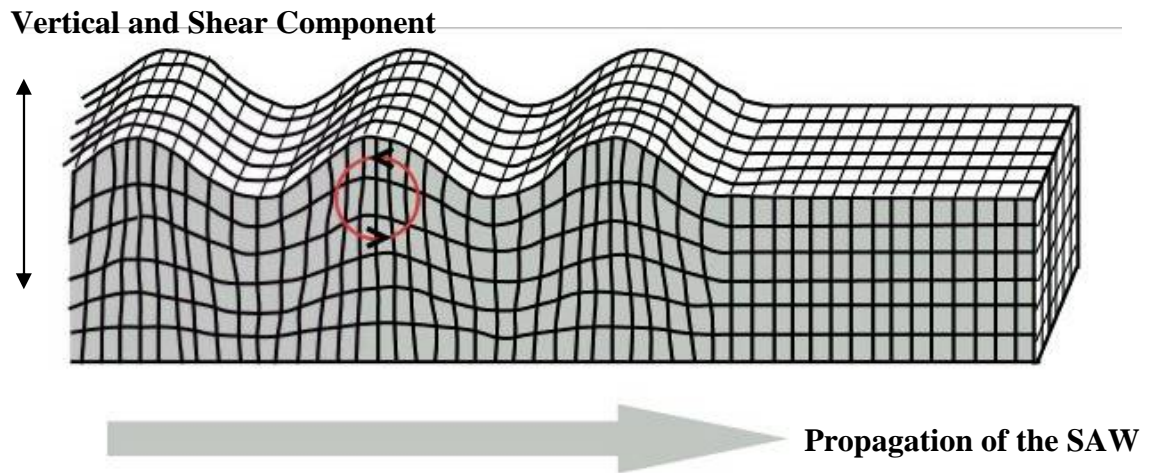
Figure 2.1: Schematic of Rayleigh mode SAW propagation[37]

This amplitude and frequency can couple with a medium placed in contact with the device's surface since Rayleigh waves have all their acoustic energy confined within one wavelength of the surface. Such coupling between the surface of the

sensor and external media strongly affects not only the amplitude, but also the velocity of the wave. This feature enables SAW sensors to directly sense mass and mechanical properties of the contact media, such as shear modulus and thermal expansion coefficient. One of the disadvantages of the Rayleigh mode of SAW is that because the wave is a surface-normal wave, it makes the SAW device poorly suitable for liquid sensing application. When the Rayleigh mode SAW sensor is contacted by a liquid, compression waves are created, causing an excessive attenuation of the acoustic wave. As a result, Rayleigh mode SAW sensors are usually used for dry environmental sensing, such as temperature and pressure sensors[38].

On the other hand, if the cut of the piezoelectric crystal material is rotated appropriately, the wave propagation mode changes from a vertical shear SAW sensor to a shear-horizontal surface acoustic wave (SH-SAW) sensor[39], as shown in Figure 2.2. A.E.H. Love predicted the existence of the SH-SAW wave mathematically in 1911. The lattice motion of a Love wave forms a horizontal line perpendicular to the direction of propagation (i.e. are transverse waves). Hence, it is very critical to deposit a highly oriented c-axis piezoelectric material to generate a Love mode SAW[40]. When the SAW IDT is aligned perpendicular to the c-axis of the piezoelectric material, Love mode waves are predominantly generated. This Love mode SAW dramatically reduces the losses when liquids come in contact with the propagating medium, which allows Love mode SAW sensors to be used as biosensors[41].

Shear Horizontal Component

Propagation of the SAW
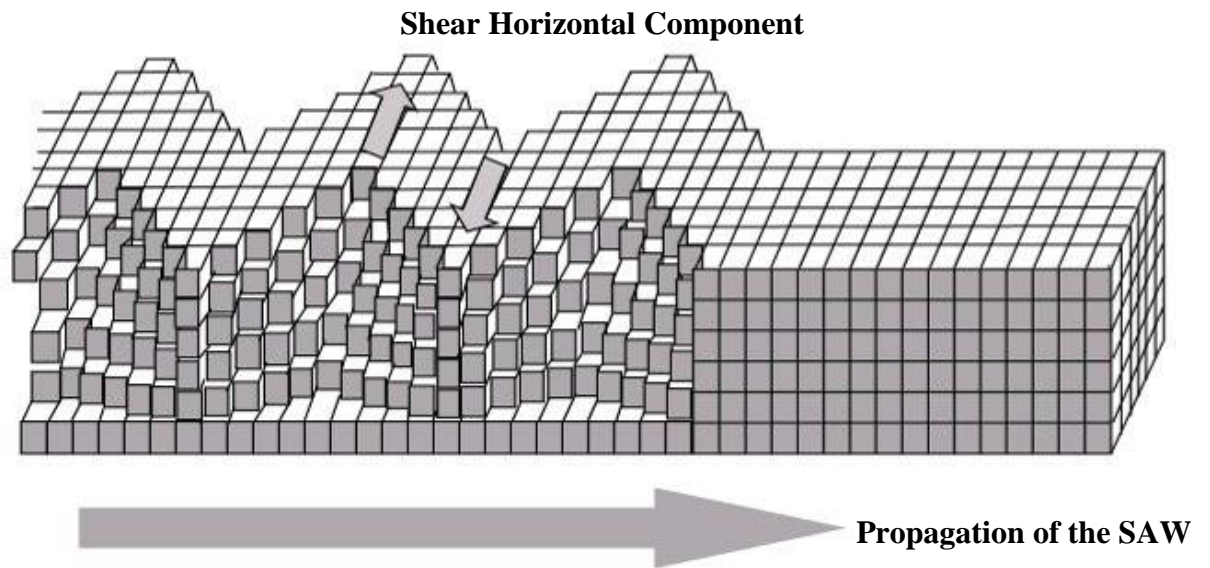
Figure 2.2: Love mode SAW propagation[30]

Love wave devices also offer the advantage of concentrating the acoustic energy in the guiding layer grown on an appropriate substrate, thus offering the opportunity of higher mass sensitivities. Several Love mode SAW sensors operating in both gaseous and liquid media have been demonstrated[42, 43].

2.3   Piezoelectric Material for SAW Sensor

A SAW is generated on the piezoelectric material which operates at a high frequency oscillation governed by the design of the IDT. To obtain the maximum acoustic wave energy from the input electrical energy, the deposition of a high piezoelectric coefficient material as a substrate is the most important parameter of the SAW sensor as well as its high quality deposition method[44, 45]. The piezoelectric coefficient is defined as the ratio between mechanical energy and electrical energy[46].

$$K^2 (piezoelectric\ coefficient) = \frac{acoustic\ energy}{electrical\ energy} \quad (6)$$

ZnO is a piezoelectric material with the highest piezoelectric efficiency along with Lithium Niobate (LiNbO3)[47]. Another advantage of ZnO is biocompatibility[48]. Due to the biocompatibility of ZnO, many biomedical devices have used this material for a medical device[49]. Moreover, ZnO can be grown by thin film deposition methods, such as RF sputtering and pulsed laser deposition (PLD) with low limit of the substrate[50, 51]. A high quality ZnO thin film deposition process is well developed and compatible with traditional photolithography techniques. Pulsed laser deposition (PLD) is one of the common ZnO deposition methods for high quality deposition[52,53]. PLD has several advantages and benefits over other growth techniques, including high control over growth parameters, fast growth rates, and low growth temperatures. Because of its relatively simple set-up and operation, it has been widely used in research. ZnO with a high piezoelectric coefficient is capable of generating very high frequency (GHz) SAW and when combined with a SiO_2/Si substrate it can be an excellent material choice for Love mode propagation [54]. Based on its piezoelectric properties, biocompatibility, and the high quality fabrication process, ZnO is the best candidate piezoelectric material for the implantable sensor design.

2.4   Interdigitated Transducer

The operational frequency of the SAW sensor for future implantable applications is set by the Federal Communication Commission (FCC), which allows from 401 MHz to 406 MHz for Medical Device Radiocommunications Service (MedRadio). Based on the SAW velocity in our ZnO film (4812 m/s) and the fact that half of the SAW wavelength is equal to the separation of each electrode pair, the separation length of the IDT has to be 6 μm in order to achieve a 402 MHz operational frequency for the SAW sensor.

The IDT material is also crucial since the IDT can induce the energy insertion loss from the input electrical energy to the piezoelectric substrate. The energy insertion loss depends on the acoustic impedance and spacing distance of the IDT electrode width. Some potential materials for the IDT are compared based on the acoustic impedance matching theory and reflective coefficient equation[55], as shown in (7) and (8).

$$Z = \rho \cdot \upsilon = (density) \cdot (velocity) \qquad (7)$$

$$R = \frac{P_1}{P_0} = \left(\frac{Z_2 - Z_1}{Z_2 + Z_1} \right)^2 \qquad (8)$$
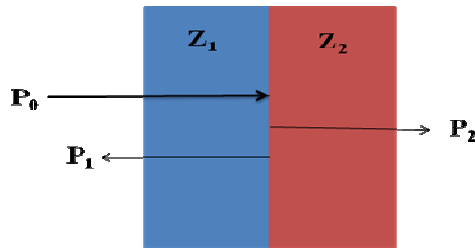
Figure 2.3: Schematic of the two layers acoustic impedance match

where Z is the acoustic impedance, ρ is the density of the layer, v is the acoustic velocity of the material, R is the acoustic wave reflective coefficient, P_0 is the incident power, P_1 is the reflective power, P_2 is the transmission power, Z_1, and Z_2 are the acoustic impedance in each layer respectively. Aluminum and gold are selected as the IDT material and their properties were calculated based on equation (7) and (8). The results are shown in table 1.

R	Aluminum (Al)	Gold (Au)
Acoustic Wave Reflective Coefficient	0.058	0.012

Table 1. Acoustic wave reflection coefficient calculation results

Based on the calculation results, Au was chosen as the material for the IDT.

In addition to the acoustic impedance matching, the width of the electrode in the IDT also affects the energy insertion loss of the sensor[56]. Generally, the electric field in the piezoelectric material by the IDT is proportional to the width of the gap, g in Figure 2.4, between an electrodes pair.
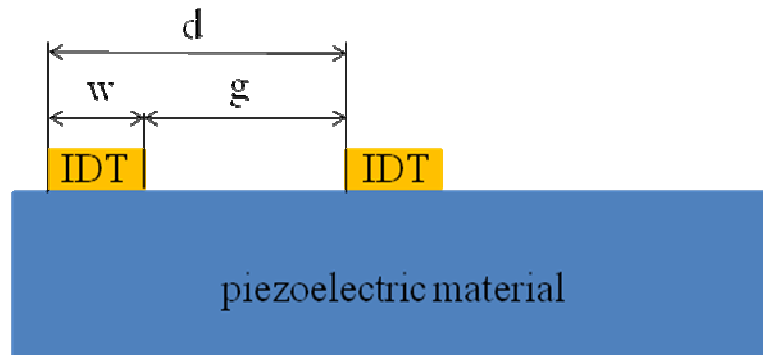
Figure 2.4: Cross sectional view of the IDT in the SAW sensor

where d is 6 μm in this SAW sensor design, w is the width of the electrode, and g is the gap between two electrodes. If the width of the electrode, w in Figure 2.4, becomes narrower, more of the electric field affects the piezoelectric substrate, so the efficiency of the mechanical displacement is increased.

In this work, three different widths of IDT electrodes were designed, including 1 μm, 1.5 μm, and 2 μm, to investigate the electrode width dependence of the energy insertion loss.

2.5   Design of the SAW sensor

The PLD method for ZnO deposition introduces a specific frequency pulsed laser to the target, and the material is deposited on the sample. Because of the simple set up and very close lattice structure similarity between the target and deposited films, PLD is an optimal tool for high quality thin ZnO deposition. However, PLD allows a good uniformity only in die level deposition, because the laser cannot cover wide areas in the target uniformly. Thus, it requires chip level rather than wafer level processes.

Because of this limited uniformity of the PLD, an inverted SAW sensor was designed as shown in Figure 2.5. Compared with the traditional SAW structure in Figure 2.5(a), where the IDT is patterned over the piezoelectric material, in this work the IDT is patterned under the piezoelectric film in the inverted SAW sensor.
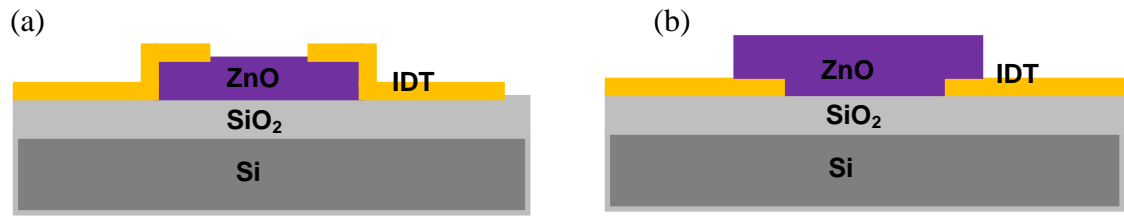
Figure 2.5: (a) Traditional SAW sensor cross sectional view,
(b) Inverted SAW sensor for PLD ZnO deposition cross sectional view

The traditional SAW sensor can achieve higher sensitivity than the other design, because an additional mass loading affects the SAW propagation directly[57]. However, it is difficult to deposit high quality ZnO on the entire wafer for the traditional SAW structure using PLD. A piezoelectric substrate is generally used for the SAW sensor fabrication rather than piezoelectric thin film SAW. There can be also corrosive effect on the IDT, since the IDT exposed to the external environment directly.

In the inverted SAW sensor design, the SAW, which is generated in the IDT, can disperse from between bottom and the top of the piezoelectric thin film area, so the sensitivity of the sensor would be decreased in the same traditional SAW sensor structure based on the inverse relation between the sensitivity and SAW velocity dispersion ratio[58]. However, the maximum acoustic energy of the Love mode SAW is inside of the piezoelectric film at about 5% of the SAW wavelength depth (600 nm in this SAW sensor). Therefore, the inverted SAW sensor still can achieve the same level of the sensitivity compared with the traditional SAW structure due to the maximum energy Love mode wave location. In addition, the inverted SAW sensor is still able to detect biofilm formation, since the mass loading due to the biofilm

formation is usually 100 - 600 μg. The advantages of this revised structure also include the reduced possibility of IDT corrosion than the traditional SAW structure because IDT is covered by ZnO film. Furthermore, this new structure is compatible with the PLD for ZnO film deposition, which allows a high quality and specific lattice structure deposition.

2.6   Passivation of the SAW sensor

ZnO is soluble when in contact with a non-neutral pH liquid or after long term moisture exposure[37]. Zinc (Zn) has less ionization energy, which is the minimum required energy to become an ion, than hydrogen (H). As a result, if Zn and H are in the same solution, Zn will be ionized in the solution due to the smaller ionization energy than H resulting with generation of hydrogen gas. Because of this solubility of ZnO, a SAW sensor based on ZnO is challenging for biosensor applications[59, 60]. Specifically in this work, when the ZnO film was placed in the bacterial growth media without a passivation film, the ZnO layer was dissolved completely in three hours. Therefore, the ZnO film-based SAW sensor for biosensor applications had to be passivated by a dielectric thin film without a significant loss of the sensitivity. Since the SAW propagates on the surface of the sensor, the mechanical properties of the passivation film, such as shear modulus and density, are critical parameters to passivate the sensor without losing in sensitivity due to the mismatch in material properties. To study the sensitivity dependence in different passivation materials, a

theoretical model for the biofilm SAW sensor was developed, as shown the schematic

of the cross sectional view of the model in Figure 2.6.
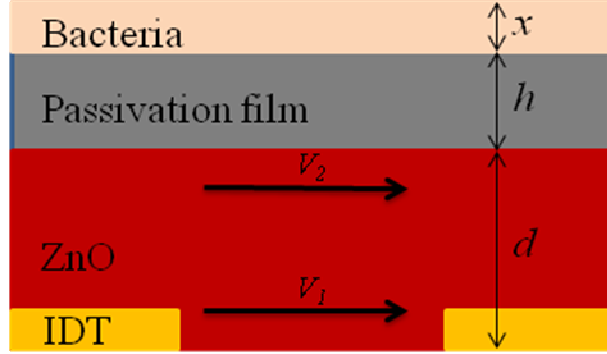
Figure 2.6: Schematic of passivation SAW sensor for biofilm detection[61]

where x is the biofilm thickness, h is the thickness of the passivation film, and d is

ZnO film thickness. The bacterial growth over the sensor was assumed to be uniform,

so that mass loading depends only on the thickness of the biofilm (x). In addition, the

SAW velocities were assumed to be equal both in the bottom and top ZnO layers,

yielding $V_1 = V_2$ as in Figure 2.6 to simplify the model calculation.

The mass sensitivity of the SAW sensor is given in equation (9)[14].

$$S_m^v = \lim_{\Delta m \to 0} \frac{1}{\Delta m} \left(\frac{\Delta v}{v_0} \right) \tag{9}$$

where S_m^v is the mass sensitivity of the SAW sensor, v_0 is the initial SAW velocity

before mass loading, Δm is the amount of the mass loading, and Δv is the SAW

velocity change due to the mass loading. Based on the uniform bacteria growth

assumption and from equation (9), a one dimensional mass sensitivity for the SAW

sensor can be derived as shown in equation (10).

$$S_m^v \propto \frac{dv}{dx}_{x \to 0}$$

(10)

where x is the bacterial biofilm thickness. The velocity of the SAW is derived by the

three dimensional acoustic wave equation as shown in equation (11)[14, 62].

$$v = \sqrt{\frac{C}{\rho}}$$

(11)

where v is the SAW velocity, C is the shear modulus, and ρ is the density of the

surface. The acoustic wave velocity in the passivated SAW sensor can be defined as a

function of passivation film thickness (h), density (ρ), and biofilm thickness (x) for

non-passivated and passivated SAW sensors by (12) and (13), respectively.

$$v = \sqrt{\frac{C_{ZnO}}{\rho_{ZnO} + \rho_{bac}}} = \sqrt{\frac{C_{ZnO}}{\rho_{ZnO}} \left(\frac{1}{1 + \frac{\rho_{bac}x}{\rho_{ZnO}d}} \right)}$$

(12)

$$v = \sqrt{\frac{C_{ZnO}}{\rho_{ZnO}} \left(\frac{C_{film}}{C_{ZnO} + C_{film}} \right) \left(\frac{1}{1 + \dfrac{\rho_{film}h}{\rho_{ZnO}d} + \dfrac{\rho_{bac}x}{\rho_{ZnO}d}} \right)} \qquad (13)$$

where C_{film} is the shear modulus of the passivation film, h is the thickness of the film, and d is the thickness of the ZnO, as shown in Figure 2.6. In the passivated SAW sensor calculation, the total shear modulus, including ZnO and passivation film, was calculated by the series mechanical spring model, since the mechanical displacement in the IDT is transferred from the ZnO film to the passivation film sequentially. In equations (12) and (13), the key variable for the velocity is bacterial biofilm thickness (x), and the other parameters can be determined to optimize the sensitivity of the sensor. Some potential passivation materials, such as silicon nitride, aluminum oxide, and silicon dioxide, were selected based on the mechanical properties similarities to ZnO film and also water resistivity. The mechanical properties of the potential materials are summarized in table 2. Using these parameters and equation (13), the velocity function was defined depending on the biofilm thickness. The normalized velocity in each material was plotted according to the biofilm film thickness change as shown in Figure 2.7.

	Shear modulus (C_{film})	Poisson ratio	Density (ρ_{film})
ZnO	44.28 GPa	0.30	5.606 g/cm^3
Si$_3$N$_4$	80.60 GPa	0.24	3.290 g/cm^3
SiO$_2$	32.19 GPa	0.17	2.606 g/cm^3
Al$_2$O$_3$	124.0 GPa	0.21	3.950 g/cm^3
Teflon	0.005 GPa	0.46	2.199 g/cm^3

Table 2. Potential passivation film material properties [63, 64]
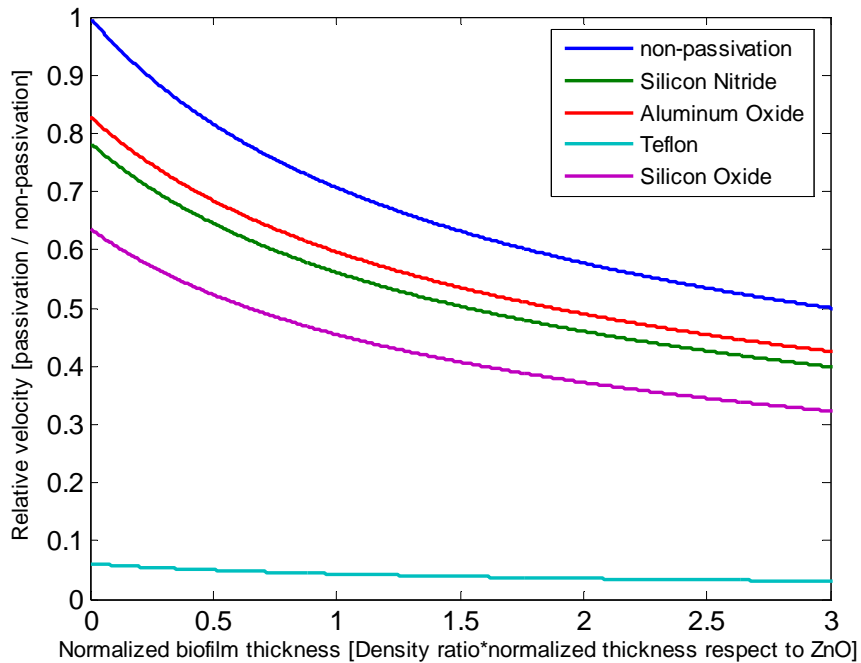
Figure 2.7: Relative SAW velocity from some candidate materials

Compared with a non-passivated SAW sensor, the velocity in the passivated SAW

sensor was always more attenuated due to the passivation film mass loading and

mismatch in mechanical properties as shown in Figure 2.7. Moreover, the relative sensitivity of the passivated SAW sensor can be calculated by the fact that the sensitivity is proportional to the SAW velocity change during the biofilm growth which corresponds to the slope of the curve as shown in Figure 2.7. The differentiated plot (relative sensitivity change) of Figure 2.7 is shown in Figure 2.8.
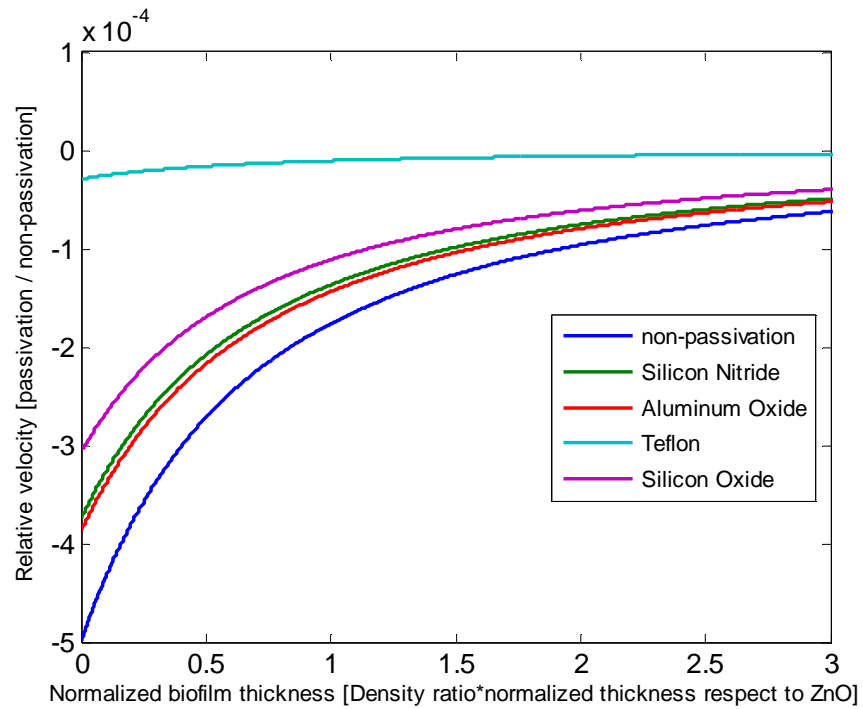
Figure 2.8: SAW sensor sensitivity from candidate materials

In Figure 2.8, the normalized sensitivity for the potential passivation materials was the y axis intercept, since that is the point described in equation (10) where biofilm (x) approaches zero. The theoretical normalized sensitivity of SAW sensors passivated with different films (y axis intercepts in Figure 2.8) are shown in Figure 2.9.
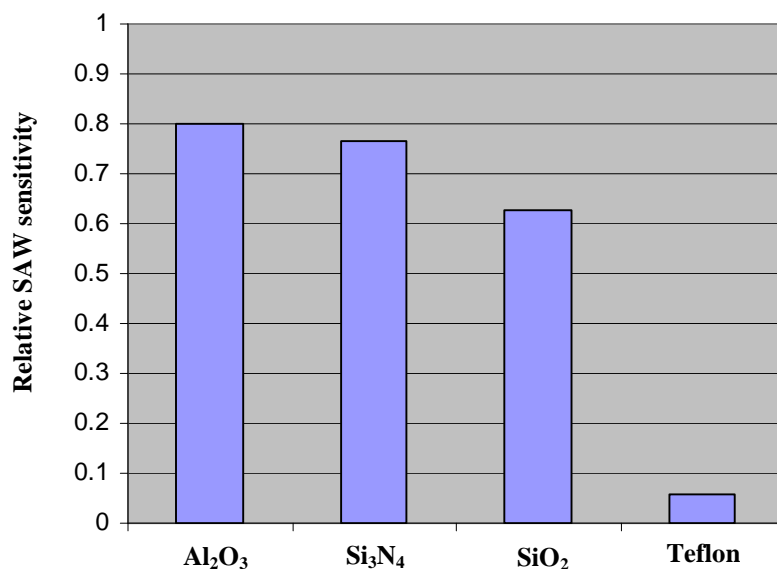
Figure 2.9: Normalized sensitivity from different passivation SAW sensors

Based on the modeling calculation, Aluminum Oxide passivated SAW sensor showed better sensitivity than other materials, and Teflon was the worst choice for this application, even though Teflon is one of the most common biocompatible materials for biomedical applications. Silicon nitride and aluminum oxide were chosen as potential passivation films for the SAW sensor since the theoretical normalized sensitivity calculation results were different only 2%. The schematic of the passivated SAW sensor is shown in Figure 2.10.
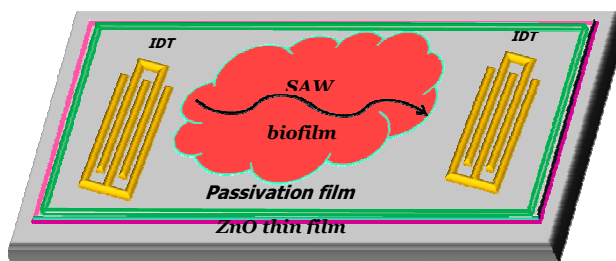
Figure 2.10: Schematic of the passivated SAW sensor

3. Device Fabrication

3.1   Process Flow

The overall fabrication process is shown in table 3.

Process Step	Process Description	Cross Sectional View
SiO$_2$ Deposition	LPCVD 60 nm at 150 °C	
Pattern IDT (AZ5214)	AZ 5214 image reversal pattern	
Cr/Au deposition	Cr/Au (15nm / 200 nm) E-beam evaporation deposition	
Lift off	Ultrasonication in acetone	
Dice wafer		
ZnO deposition (400 nm)	KrF excimer laser at a wavelength of 248 nm with pulse duration of 25 ns at 250 °C	

ZnO pattern	H$_3$PO$_4$ + Acetic acid + DI water for 40 seconds (1:1:30 dilution by volume)	
Annealing	800 °C for 1 hour (ramp up for 1 hour, cool down)	
Passivation film deposition **(Al$_2$O$_3$ 45nm)**	Al$_2$O$_3$ ALD deposition at 150 °C	
Open electric pads	H$_3$PO$_4$ + Acetic acid + DI water (1:1:30 dilution by volume)	

■ Si   ■ SiO$_2$ ■ ZnO   ■ Cr/Au   ■ Al$_2$O$_3$

Table 3: Fabrication process flow

3.2   SiO$_2$ Deposition

The SAW velocities in the ZnO film and Si substrate are different, 4812 m/s and 5840 m/s respectively. In addition to the non-piezoelectricity of silicon, this acoustic velocity mismatch between the Si substrate and ZnO film can cause a significant acoustic wave loss due to the loss of the SAW from the ZnO to the Si substrate. Therefore, a thin layer of SiO$_2$was deposited between the ZnO and Si to prevent the loss of the SAW. The thickness of SiO$_2$ layer is optimized to minimize the acoustic wave loss and strain in two layers[41]. The 60 nm SiO$_2$ was deposited by low pressure chemical vapor deposition (LPCVD) at 150 °C on 4 inch p-type (100) silicon wafer.

3.3   Interdigitated Transducer Pattern

IDT was patterned on the SiO$_2$/Si layer before depositing ZnO. Three different IDT electrode widths (1, 1.5, and 2 µm) were designed to investigate the energy insertion efficiency dependence on the electrode width variation. The energy insertion efficiency is known since the insertion efficiency is inversely proportional to the IDT electrode width.

16 devices with three different IDT electrodes on a 4-inch wafer were designed. The designed chrome mask for IDT is shown in Figure 3.1. To make easy electrical contact in the device package, the gold electric pads were expanded by 2 mm by 2mm. The overall device dimensions including the extended electrical contact pads was 1 cm by 3 cm.
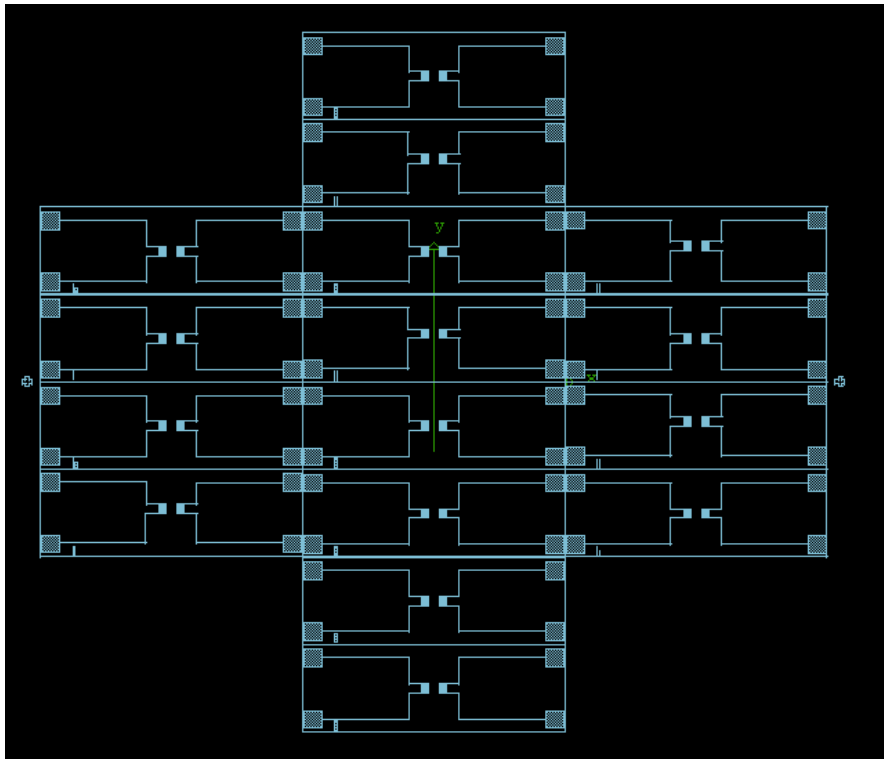
(a) Mask layout on 4-inch-wafer
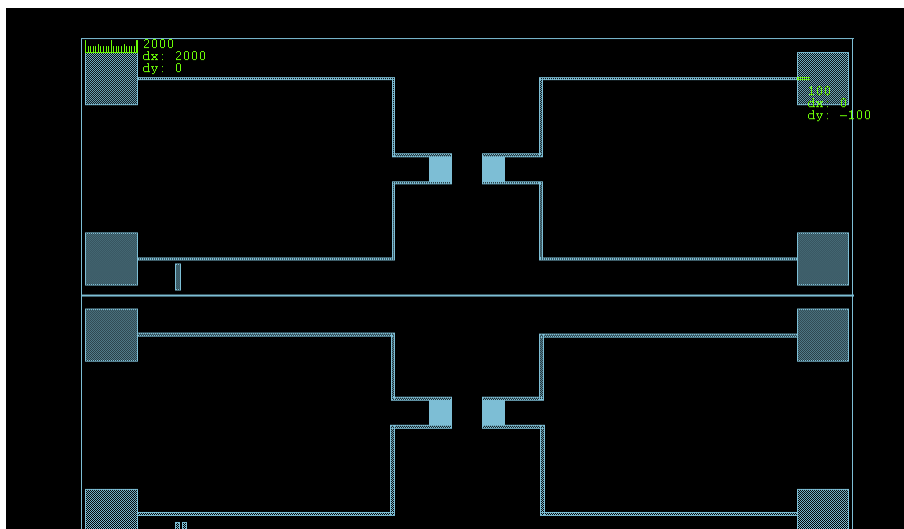
(b) Mask layout in device (1 μm IDT SAW sensor)
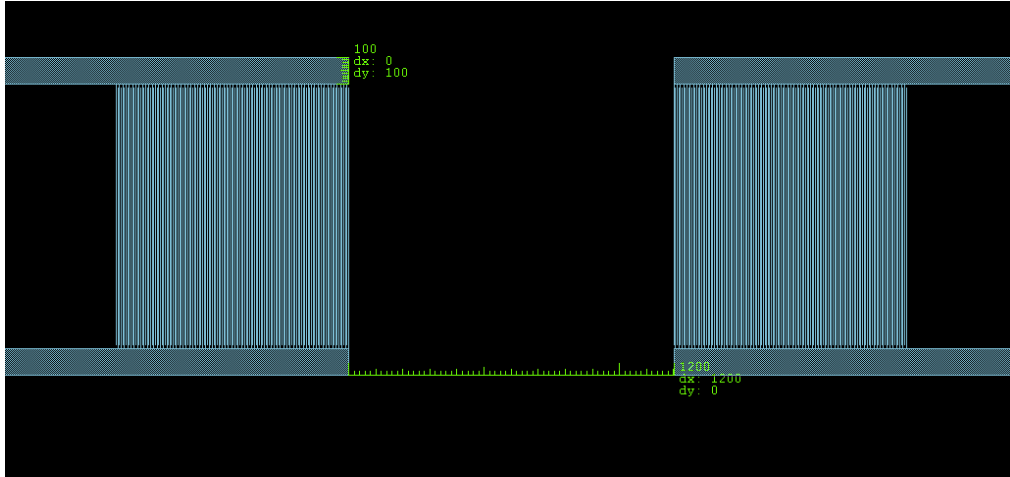
(c) Mask layout in the IDT area
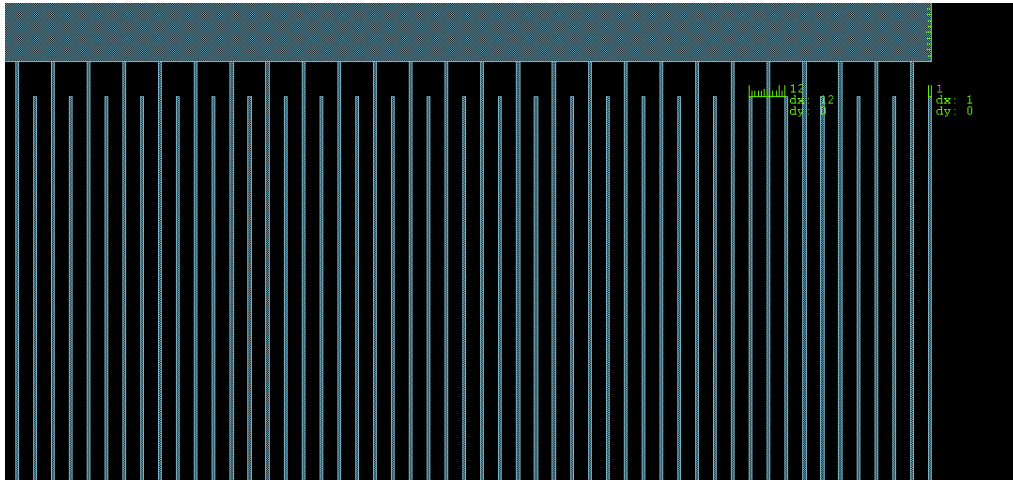
(d) Mask layout in the IDT

Figure 3.1: Mask layout for the SAW sensor

The traditional projection photolithography was used to pattern the IDT using AZ5214 photoresist. The AZ5214 photoresist was spun at 3000 rpm for 30s, and baked for 1 minute at 100 °C. The resist was exposed using a dose of 63 mJ/cm^2 at 405 nm and then the wafer was baked for 45s at 125 °C. After the postbake, the

wafer was flood exposed by the UV light for 2 min, providing a dose of about 2160

mJ/cm^2. Finally the wafer was developed for 2 minutes in AZ400K : Deionized

water at a ratio of 1:6. The microscope image after the lithography is shown in

Figure 3.2.
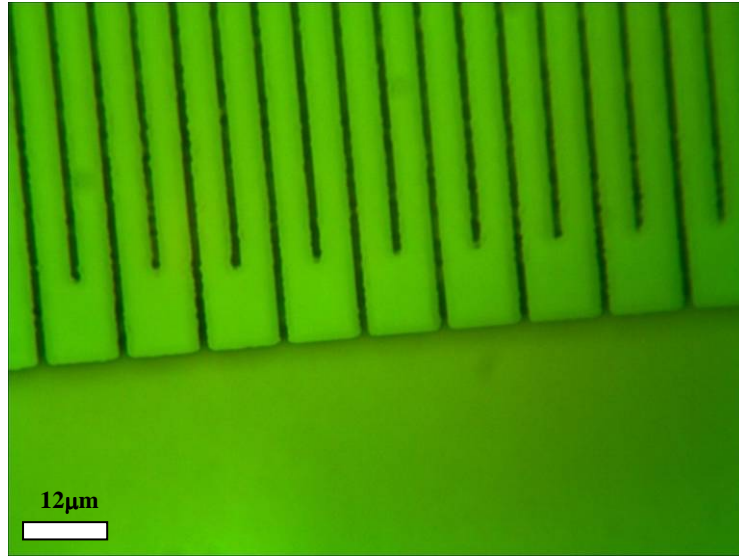
Figure 3.2: Microscopy image of the 1 μm IDT pattern after photolithography for 1 μm IDT SAW sensor

As shown in Figure 3.2, the IDT pattern was not clear after the photolithography

because of the limited resolution of the contact lithography at 1 μm feature sizes.

To remove the photoresist residue, Oxygen (O_2) plasma was used for 50 s at 150 W

RF power. After O_2 plasma, the IDT pattern is shown in Figure 3.3.

12μm
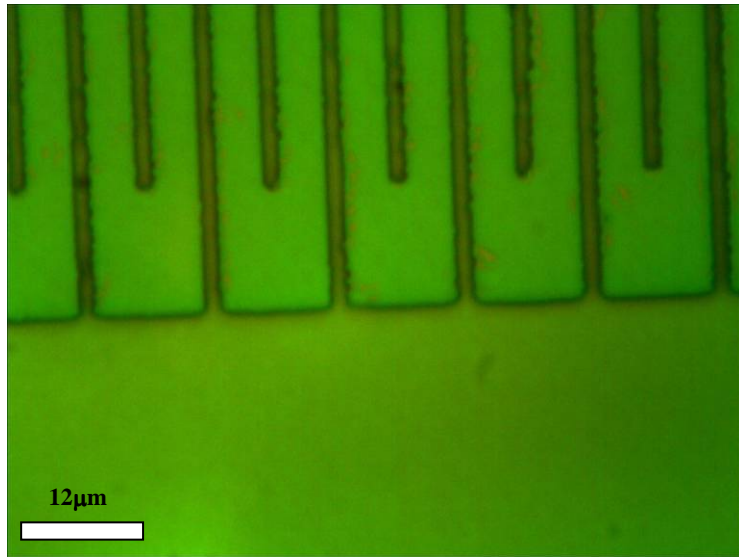
Figure 3.3: After O$_2$ plasma for 50 s at 150 W in 1 μm IDT SAW

Then, the Cr/Au (15nm/200nm) was deposited by E-beam evaporation, and followed by lift-off of the photoresist in acetone using an ultrasonic bath. The Cr/Au patterned IDT is shown in Figure 3.4.

50 μm
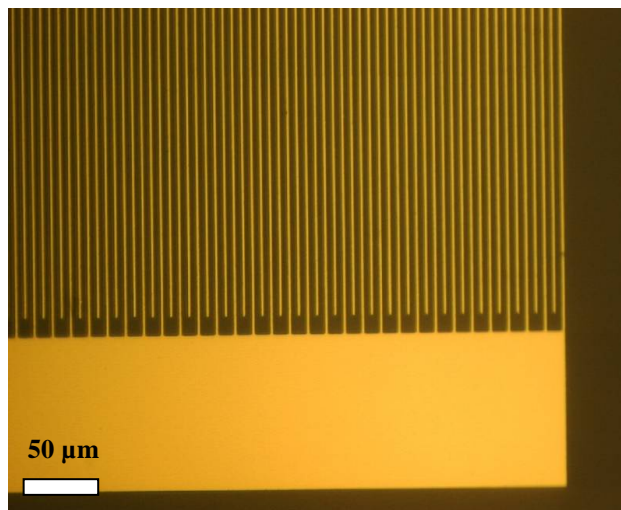
Figure 3.4: Optical microscope image of the Cr/Au (15nm/200nm) patterned IDT

3.4   ZnO Deposition

After patterning IDT, the wafer was diced for the ZnO deposition by PLD. The laser deposition system used a KrF excimer laser at a wavelength of 248 nm with pulse duration of 25 ns to ablate a high purity (99.99%) ZnO ceramic target. The ZnO was grown at 250° C with an ambient oxygen partial pressure of ~1.0×10^{-4} Torr. The thickness of ZnO film was 400 nm.

3.5   ZnO Pattern and Annealing

To open the electric contact pads from ZnO, the ZnO was patterned using a mixture composed of phosphorous acid, acetic acid and DI water (1:1:30). To protect the sensing area from the etchant, a drop of photoresist was placed in the IDT area and baked for 5 min since the ZnO pattern was not critical as long as the ZnO film remained in the IDT area. Then, the chip was placed into the ZnO etchant for 40 s. After patterning ZnO, the photoresist was removed with acetone.

The resistance of the IDT was measured after opening the electric contact pads. In the ideal case, the resistance in the IDT would be infinite since the interdigitated electrodes are open circuit and SiO_2 is an insulator. However, the resistance of the IDT was about 100 Ω in both input and output IDTs.

The main reason of the low resistance in the IDT may be because of the high quality of PLD ZnO, which implies the number of the ZnO single lattice domain is small, and thereby the electrical resistance is low. The resistance of the ZnO film depends on the number of the ZnO single lattice domain, which is pure crystal ZnO

area with boundary in each domain. This low resistance IDT cannot induce the strong electric field, because of the low potential difference. As a result, the SAW may not be able to be generated on the surface due to the low potential energy between the two electrodes of the IDT. One of the effective ways to increase the resistivity of ZnO film is annealing at a high temperature[65]. The annealing can help to reorganize the lattice structure and also make smaller domains, so the number of boundaries in the domains is increasing. The SAW device was annealed at selected temperatures and the resistance was measured after the annealing. The resistance result after annealing at different temperature is shown in table 4.

Device	Non-annealed	330 °C	800 °C
1 μm SAW	150 Ω	450 Ω	> 30 MΩ
1.5 μm SAW	150 Ω	500 Ω	> 30 MΩ
2 μm SAW	120 Ω	NA	26 MΩ

Table 4: Resistance measurement after ZnO annealing at 330°C and 800°C

At first, the device was annealed at 330˚C to investigate the resistance difference after low temperature annealing. As shown in table 2, even if the temperature was at 330°C, the resistance increased about three times compared with non-annealed ZnO film resistance. In the 800°C annealing process, the temperature was increased 13˚C/min for one hour from room temperature to 800˚C, and annealed for one hour

at 800˚C. Then, the chip was allowed to cool down overnight. After 800˚C annealing for one hour, the resistance of the IDT was out of measurable range (> 30MΩ) by the multimeter. The high resistivity of ZnO resulting from the annealing at 800˚C can induce a strong electric field in the IDT due to the high potential difference. As a result, the mechanical displacement can be induced efficiently, and the SAW can propagate on the surface.

3.6   Passivation Thin Film Deposition

Based on the theoretical modeling calculation, described in Chapter 2.6, Si_3N_4 and Al_2O_3 were chosen as potential passivation films for the ZnO-based SAW sensor since the normalized sensitivity difference from them in the calculation was only 2%.

40 nm of Si_3N_4 film was deposited by plasma enhanced chemical vapor deposition (PECVD) at 200 °C which is the most common deposition method for silicon nitride. Al_2O_3 film can be deposited by atomic layer deposition (ALD), or E-beam evaporation, or RF-sputtering. All three deposition methods were applied for 45 nm Al_2O_3 film deposition to investigate the fabrication process dependence in the passivation performance.

4. Testing and Results

4.1 Testing setup

4.1.1 Network Analyzer

The resonant frequency of the SAW sensor was measured by a network analyzer (HP8510, Agilent Inc., USA). The network analyzer consists of the sweeper, the test set, the vector signal processor, and the display as shown the schematic in Figure 4.1.
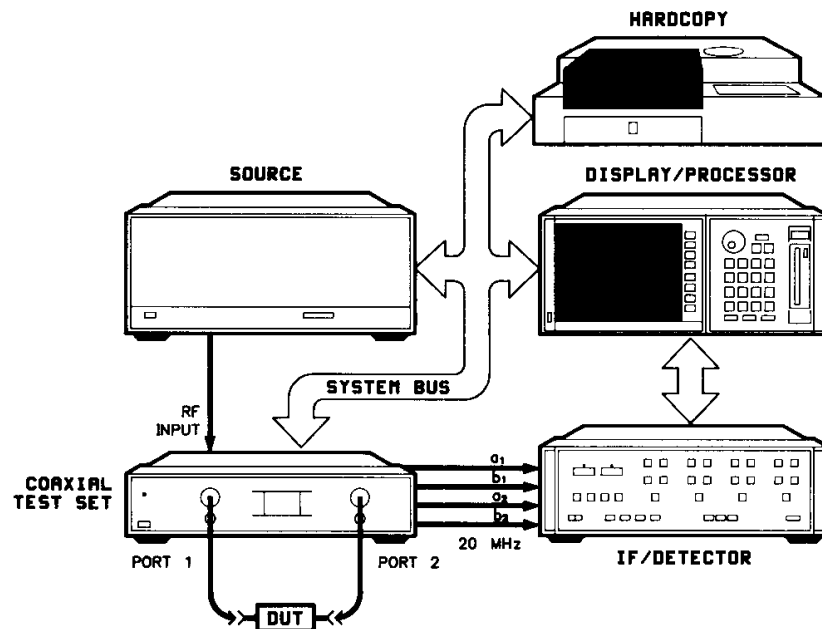
Figure 4.1: Schematic of the network analyzer [66]

The sweeper or synthesizer provides the RF stimulus to the test set from 10 MHz to 26.5 GHz. The test set supplies signal separation for the device impedance analysis, and the points at which the device under test is connected signal separation devices to analyze the device impedance. Together these comprise a complete stimulus / response test system which provides stimulus to the device under test and measures the signal transmitted through the device (S_{21}) or reflected from its input (S_{11}). The system then detects and processes the data to provide various displays showing the magnitude and phase of these responses. Accuracy enhancement techniques permit measurement calibration at the interface to the device under test, minimizing the effect of systematic measurement errors.

The network analyzer measures the four different scattering parameters (S-parameters). Many electrical properties of networks of components, such as inductors, capacitors, and resistors, may be expressed using S-parameters. For instance, the system gain, return loss, voltage standing wave ratio (VSWR), reflection coefficient, and amplifier stability can be measured by analyzing S-parameter values. The scattering refers to the way in which the traveling current and voltages in a transmission line are affected when they meet a discontinuity caused by the insertion of a network into the transmission line. This is equivalent to the wave meeting an impedance differing from the line's characteristic impedance. The schematic definition of the four S-parameters is shown in Figure 4.2.

$$S_{11} = \frac{b_1}{a_1} \qquad S_{21} = \frac{b_2}{a_1} \qquad S_{12} = \frac{b_1}{a_2} \qquad S_{22} = \frac{b_2}{a_2}$$
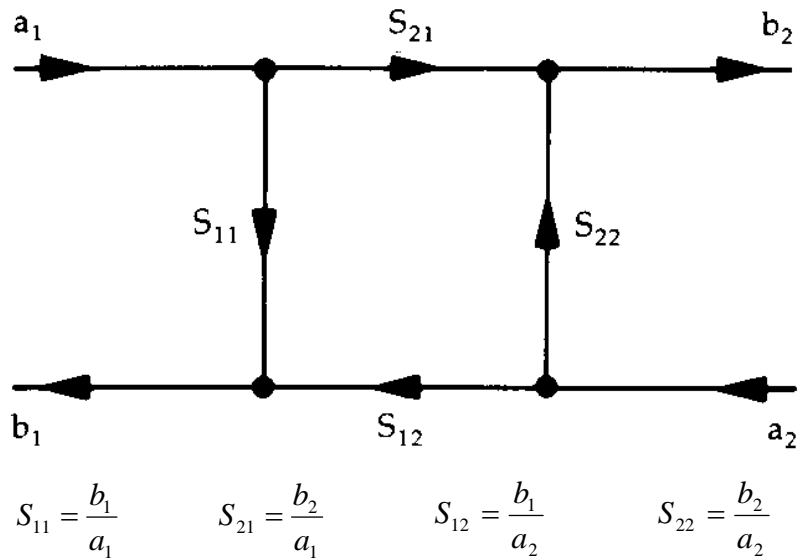
Figure 4.2: Four S-parameters in the network analyzer [61]

where a_1 is the forward reference which is provided by the synthesizer in wide frequency range RF stimulation, b_1 is the reflected signal from the testing device, b_2 is the transmitted signal through the device, and a_2 is the reverse reference from the test set. Based on these S-parameter definitions, the low peak of S_{11} at a frequency means that the least RF energy reflection occurs at the frequency. In other words, most RF energy transmits through the device because the impedance between the test device and energy source are matched. In addition, the resonant frequency of the device can be monitored by the S_{21} high peak. The S_{21} high peak at a frequency represents the transmission of the most RF energy at that frequency since the impedance is matched. Therefore, a resonant frequency of the test device can be measured by monitoring either the S_{11} low peak or the S_{21} high peak at the network analyzer.

The measured resonant frequency data was saved in the computer which communicates with the network analyzer by the general purpose interface bus (GPIB). The GPIB communication and data saving program were designed using C++ language.

Biofilm growth experiments typically span more than 48 hours, so the rate of data saving rate does not have to be fast, such as in 10 seconds rate, because the bacterial growth rate is on different order of magnitude. In addition, the only data needed to monitor the device's resonant frequency shift during bacterial growth are either the S_{11} low peak or S_{21} high peak reducing the amount of data saved as opposed to saving the entire waveform. As a result, the data saving program was designed to save only the low or high peak frequency and intensity every minute, so that it was possible to expand the experiment time without concern for the data capacity. The detailed C++ code is shown in the Appendix A.

4.1.2 Sensor Package

To make a low electrical impedance connection between the network analyzer and the SAW sensor, the package was designed with the bacterial growth well, as shown in Figure 4.3.
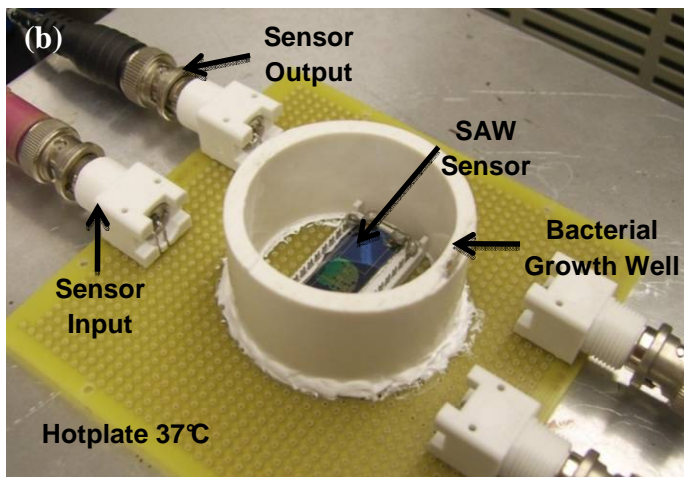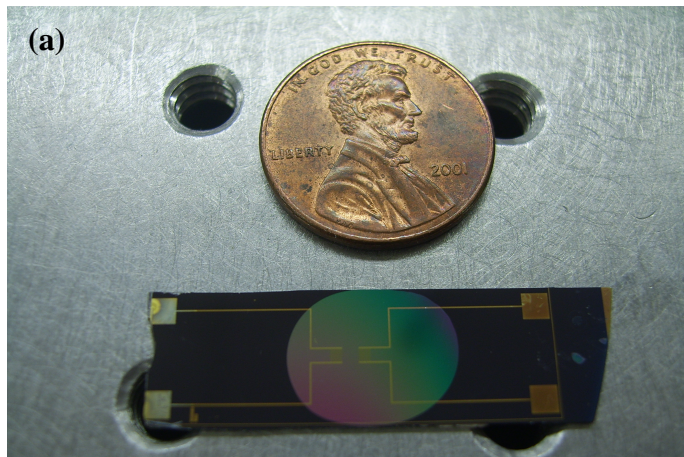
Figure 4.3: (a) Fabricated the SAW sensor, (b) the SAW sensor package for bacteria biofilm growth experiments (The input and output of the sensor are connected with the network analyzer)

The sensor had two large gold electric contact pads to make easy connection with the measurement instruments. The electrical contacts with package were made using soldering and the resistance in the package was less than 1Ω. The SAW sensor was located in the bacterial growth well, which

localized the bacterial growth and prevented growth media leakage. The network analyzer test set was connected with the SAW sensor package through low impedance BNC connection to monitor the resonant frequency of the device continuously. Finally, the package was placed on a hotplate set at 37 °C to optimize the bacterial growth and covered by a polystyrene container to reduce the temperature gradient near the testing setup.

4.2   SAW Sensor Characterization

4.2.1   ZnO Lattice Structure

For biofilm detection applications, it is critical to make sure that the propagation mode of the SAW is Love wave. This can be confirmed by investigating the lattice structure of the ZnO film. X-ray diffraction (XRD) and photoluminescence (PL) spectroscopy have been employed for structural characterization and optical evaluation of the ZnO layers.

Photoluminescence spectroscopy (PL) is a process in which a substance absorbs photons (electromagnetic radiation) and then re-radiates photons. Quantum mechanically, this can be described as an excitation to a higher energy state and then a return to a lower energy state accompanied by the emission of a photon. Depending on the material bandgap energy, the emission wavelength is different, so the material composition can be

45

investigated. After ZnO film deposition by PLD, the surface of the film was inspected by PL and the result is shown in Figure 4.4.
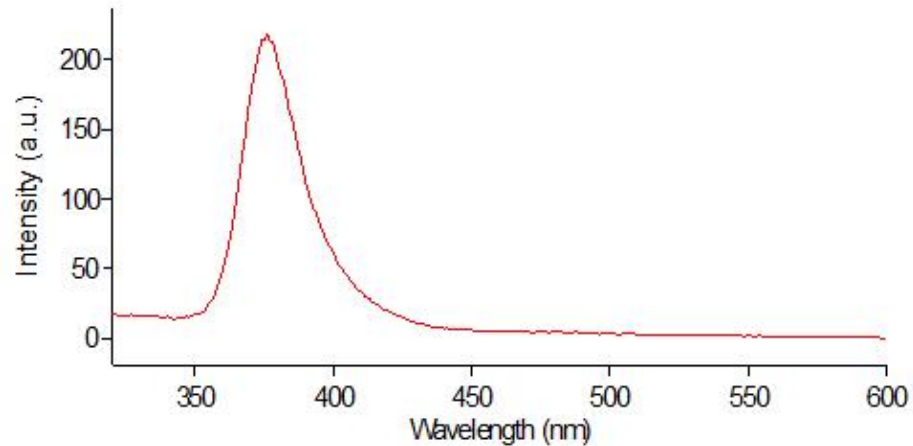
Figure 4.4: Photoluminescent spectrum of the ZnO layer, (380 nm wavelength is corresponding with the bandgap of the ZnO)

As shown in Figure 4.4, the peak wavelength of the emission light was in 380 nm. The ZnO has 3.3 eV direct bandgap, and it is corresponding to the 380 nm wavelength of the light based on the energy and wavelength relation. Therefore, this result represents the high quality of ZnO deposition since there was no other peak in the PL spectrum.

In addition, the crystal orientation of ZnO was investigated by the XRD to determine what is the preferred lattice texturing of the deposited ZnO thin film. XRD is a method of determining the arrangement of atoms within a crystal, in which a beam of X-rays strikes a crystal and diffracts into many specific directions. From the angles and intensities of these diffracted beams, a crystallographer can produce a three-dimensional picture of the density of

electrons within the crystal. From this electron density, the mean positions of the atoms in the crystal can be determined, as well as their chemical bonds, their disorder and other crystallographic, including preferred lattice orientation information. The XRD pattern of the ZnO thin film is shown in Figure 4.5.
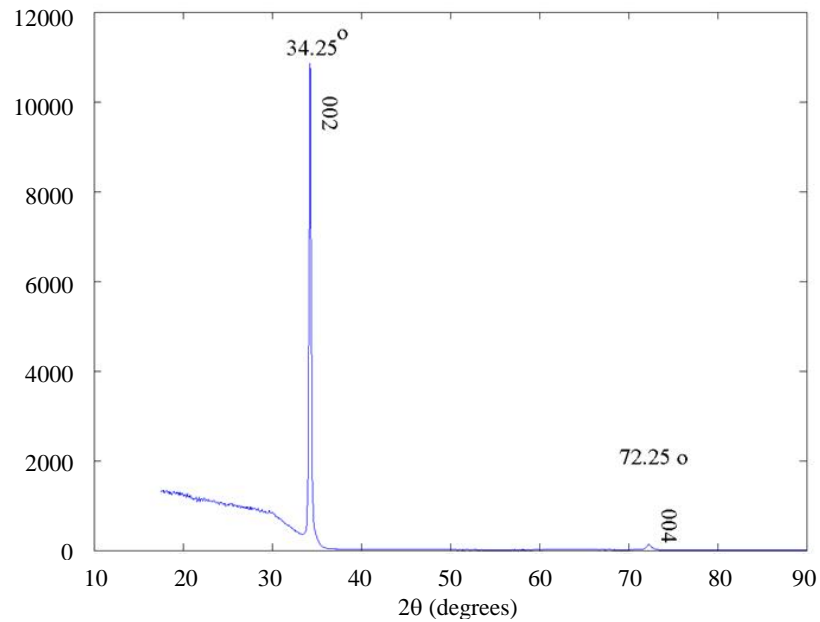
Figure 4.5: XRD pattern of the ZnO film deposited by PLD

To make sure the Love mode SAW is generated, the ZnO film should be deposited in the c-axis direction (00L) so that the c-axis of its crystal lattice is perpendicular to the substrate. As shown in Figure 4.5, the diffraction angle of the X-rays at 34.25° and 72.25° (2θ) corresponding to the (002) and (004) lattice directions, were the most intensive reflections in the PLD-prepared ZnO film.

Thus, according to the PL and XRD data, PLD-deposited ZnO thin film was single phase (no impurities) and highly structured (preferred orientation is in the (001) direction) which should provide for the generation of the Love mode SAW.

4.2.2 Passivation Film Characterization

A SAW sensor without a passivation film was placed into Lysogeny Broth (LB) bacterial growth media, which is the most common *E. coli* growth media, to study how the ZnO film withstands exposure to growth media. The pH of the prepared LB media was approximately 7.2. Based on the pH of the LB media, the ZnO should not be damaged by the solution. However, the LB media dissolved entire ZnO layer in about 3.5 hours later, as shown in Figure 4.6.
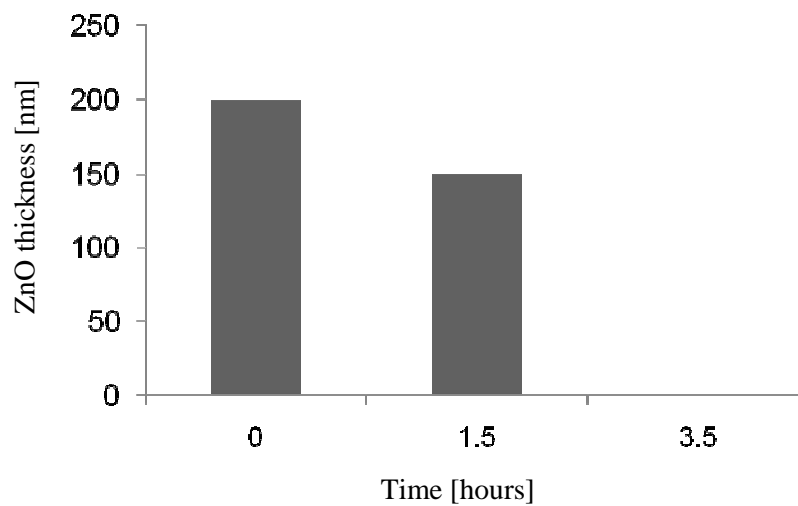
Figure 4.6: Measured ZnO thickness in LB

This result confirmed ZnO could be soluble even if it was in a neutral pH solution. To further study the ZnO solubility in solutions with close-to-neutral pH, another SAW sensor was tested in the phosphate buffered saline (PBS). Figure 4.7 shows the ZnO film thickness results in the PBS.
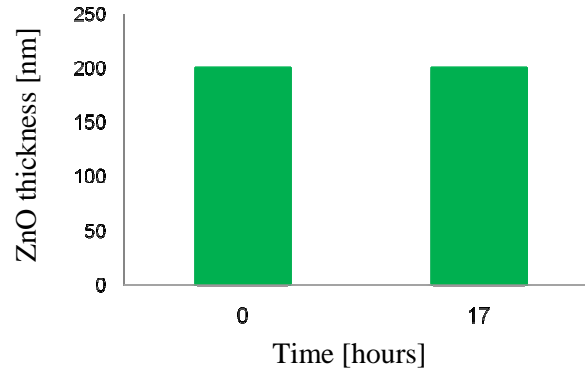
Figure 4.7: The thickness of ZnO film in PBS buffer

As shown in Figure 3.6, the ZnO film was not dissolved in the PBS. The pH of the PBS buffer was 7.4. These results confirm the dissolution of the ZnO film may be due to the composition of the LB media and not because of the pH. It may also be possible that bacterial growth media generates some ions such as chloride and hydrogen ions, that are produced by the bacterial metabolism during growth. These byproduct ions can contribute to the ZnO damage in the media.

In addition, a ZnO based SAW sensor was also tested in 10% diluted Fetal Bovine Serum (FBS), which is the most common mammalian cell culture serum due to its similarities to the *in vivo* environment. When the ZnO SAW

sensor was placed into 10% FBS with no passivation film, the entire ZnO layer was dissolved after about 6 hours.

Considering these results, a passivation thin film should be deposited on the ZnO SAW sensor for the biofilm growth experiments. For the passivated SAW sensor characterization work, a Si_3N_4 or Al_2O_3 thin film was deposited on the SAW sensor.

The Si_3N_4 film was deposited to a thickness of 30 nm by PECVD on the ZnO surface, and the passivated SAW sensor was placed in the LB media with an overnight cultured *E. coli* suspension for two days at 37°C incubation. Then, the surface of the sensor was inspected using an optical microscope, as shown in Figure 4.8.
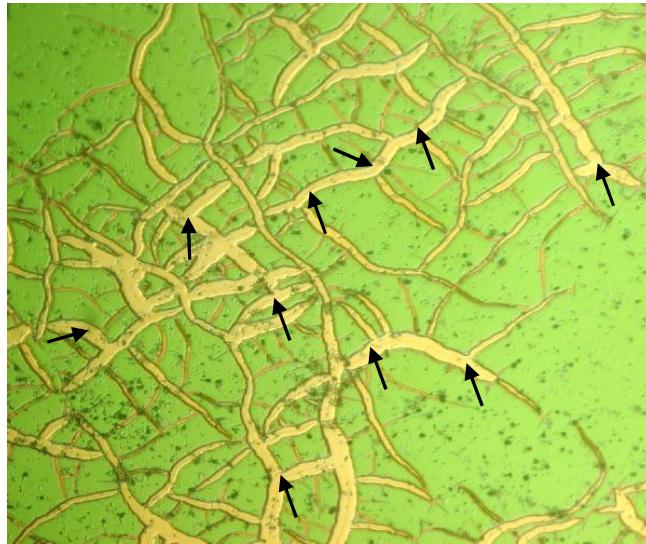
Figure 4.8: Optical image of the 30 nm thickness Si_3N_4 passivated ZnO SAW sensor after two days in LB bacterial solution (arrows indicate the ZnO damage areas)

As shown in Figure 4.8, the 30 nm Si_3N_4 could not protect the ZnO film from LB media. This might be either because of insufficiently thick Si_3N_4, or non-uniform PECVD deposition of the film in the thickness ranges used. The thickness of the Si_3N_4 film was increased to 40 nm using PECVD to study the influence of thickness on the Si_3N_4 passivation performance. However, 10 nm thickness increments of the Si_3N_4 film did not make it protect the ZnO film from the LB media as shown in Figure 4.9.
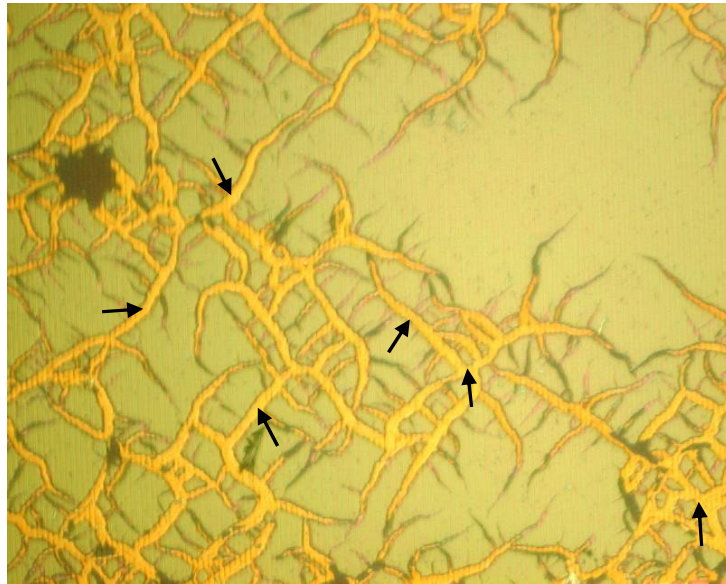
Figure 4.9: Optical image of the 40 nm Si_3N_4 passivated ZnO SAW sensor surface after two days in LB bacterial solution (arrows indicate ZnO damage)

Based on these results, the thickness of the Si_3N_4 should be more than 40 nm to be able to passivate the ZnO of the SAW sensor. However, when more than 40 nm of Si_3N_4 film was deposited, the sensor lost too much sensitivity to

use for biofilm detection applications. Thus, the PECVD Si_3N_4 was not selected to become a final passivation method for the ZnO film SAW sensor due to the non-uniform and low density film deposition provided by PECVD.

Another potential passivation film was chosen to be Al_2O_3 based on the modeling calculation presented previously. Al_2O_3 also shows high resistance to water and is used as a passivation material for other microsystem device packages[67,68]. There are many ways to deposit thin film Al_2O_3, such as evaporation, sputtering, and atomic layer deposition (ALD). RF sputtering and evaporation provide good step coverage due to high gas pressure and multidirectional deposition. ALD is the best option for the highly uniform thin film deposition due to the high level of deposition rate controllability and good coverage of high aspect ratio patterns.

The Al_2O_3 film was deposited to a thickness of 45 nm on the ZnO SAW sensor using the RF- sputtering, or E-beam evaporation, or ALD. The Al_2O_3 passivated SAW sensors were placed in LB media and 10% FBS for two days along with a prepared *E. coli* solution. The optical surface image of the Al_2O_3 passivated SAW sensor was inspected before and after the bacterial suspension experiment. Figure 4.10 shows the images of the 45 nm Al_2O_3 passivated ZnO device before the bacterial growth media characterization work using each different deposition method.
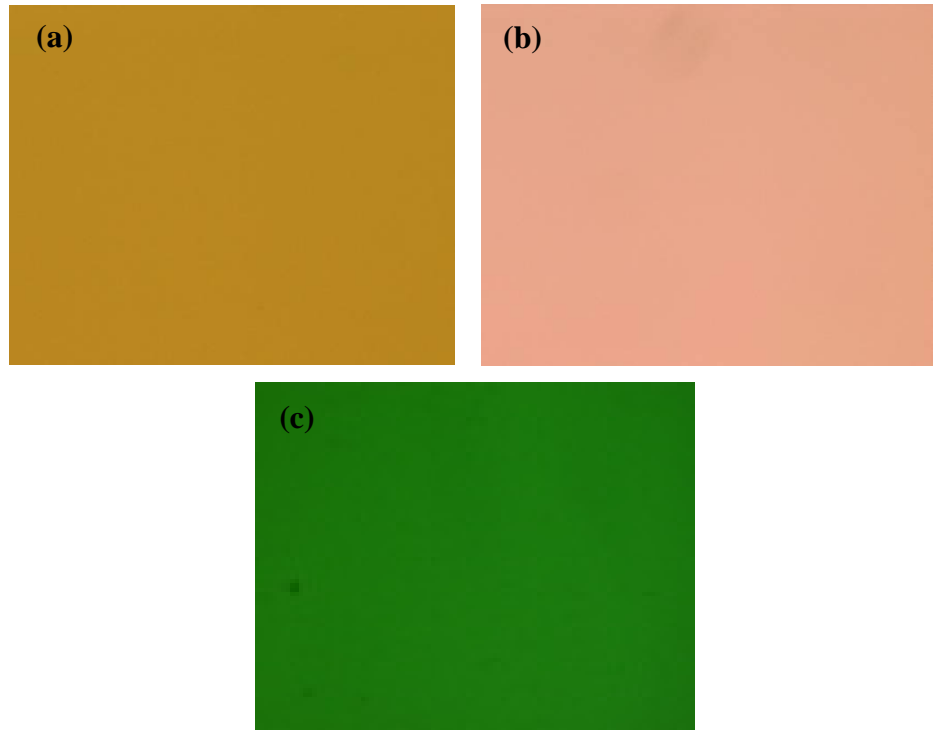
Figure 4.10: Optical surface images of the SAW sensor passivated by 45 nm Al_2O_3 deposition using (a) e-beam evaporation, (b) RF sputtering, and (c) ALD on the ZnO test chip before LB media characterization work (color difference corresponds to the ZnO thickness variance due to the optical transparency of the ZnO film.)

In Figure 4.10, since ZnO film is a transparent material, when the thickness of ZnO differs slightly between each device, the reflected color is different. While the thicknesses were not equal, all were approximately 400nm; however, the thickness of the ZnO was not a critical parameter for the passivation film characterization work.

The optical images of the Al_2O_3 film deposited by three different deposition methods for the passivation of the ZnO SAW sensor in LB media with bacterial suspension are shown in Figure 4.11.
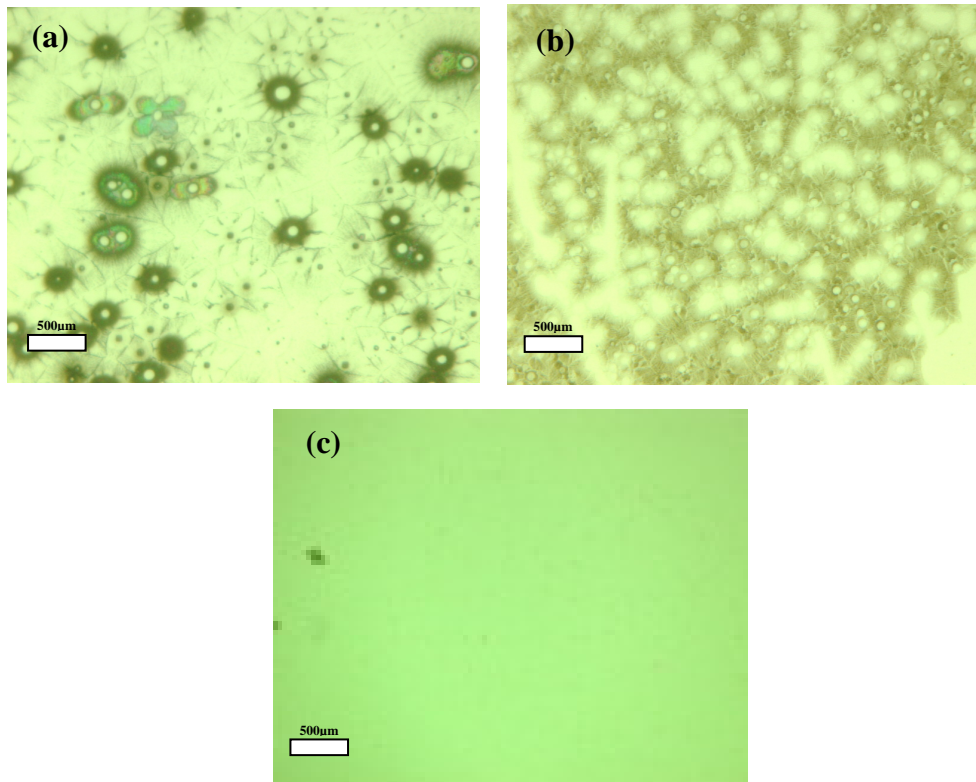
Figure 4.11: The optical surface images of the SAW sensor passivated by 45 nm Al_2O_3 film using (a) e-beam evaporation (black dot is ZnO), (b) RF sputtering (dark area is ZnO), and (c) ALD (no ZnO damage) in LB media with the bacterial solution after two days

As shown in Figure 4.11, the Al_2O_3 films deposited by RF- sputtering and E-beam evaporation were not able to provent ZnO damage from the bacterial solution. However, ALD Al_2O_3 film was able to passivate the ZnO layer from the bacterial solution. This result can be due to the highly dense thin film deposition capability of ALD.

In addition, the Al_2O_3 film passivated SAW sensors were placed in 10% FBS for investigation of the passivation performance in a different serum

using the same procedures. The surface images of the sensor after two days in

10% FBS with a bacterial solution are shown in Figure 4.12.
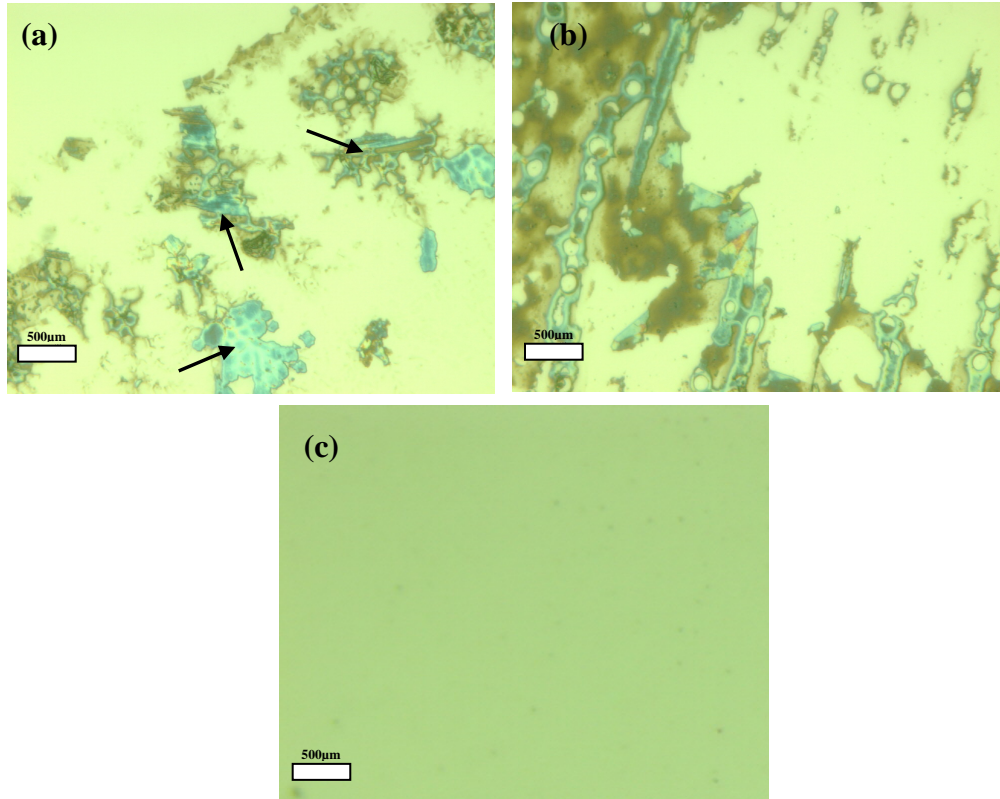
Figure 4.12: The optical surface images of the SAW sensor passivated by 45 nm Al_2O_3 film using (a) e-beam evaporation (arrow indicate ZnO residue, and bright green area is no ZnO), (b) RF sputtering (dark are is ZnO and bright green area is no ZnO), and (c) ALD (no ZnO damage) in 10% FBS for two days

The ZnO layer on the SAW sensors passivated by Al_2O_3 E-beam evaporation and RF-sputtering was dissolved by 10% FBS. However, as on the results achieved in LB media, the ZnO was protected from the 10% FBS by ALD deposited Al_2O_3.

These Al_2O_3 passivation characterization results in LB media and in 10% FBS confirmed that the only the 45 nm Al_2O_3 film deposited by ALD could passivate the ZnO film of the SAW sensor because of the highly dense and conformal film deposition of the ALD.

4.2.3 Energy Loss

To generate the SAW on the ZnO, there are several energy conversions which result in energy loss in the sensor. At first, the input AC electrical energy has an energy loss due to the acoustic impedance mismatch between IDT and ZnO at both the input and output IDT. This energy loss in the IDT and ZnO is also depending on the dimensions of the IDT electrode. The energy loss is proportional to the electrode width of the IDT [69]. In theory, if the electrode is narrow, which implies a wide gap between two electrodes, the piezoelectric material is covered by a wider electric field so the mechanical stress becomes stronger than in a narrow gap SAW sensor. There is also propagation loss depending on the quality of the ZnO. These energy losses decrease the sensitivity of the SAW sensor.

The overall energy loss can be studied by measuring the output AC voltage peak to peak (V_{pp}^{out}) versus input AC voltage peak to peak (V_{pp}^{in}). Three different IDT SAW sensors were fabricated to investigate the energy loss dependence of the IDT dimension. The V_{pp}^{out} vs V_{pp}^{in} curves for the IDT

electrodes with the different widths, 1 µm, 1.5 µm, and 2 µm are shown in Figure 4.13.
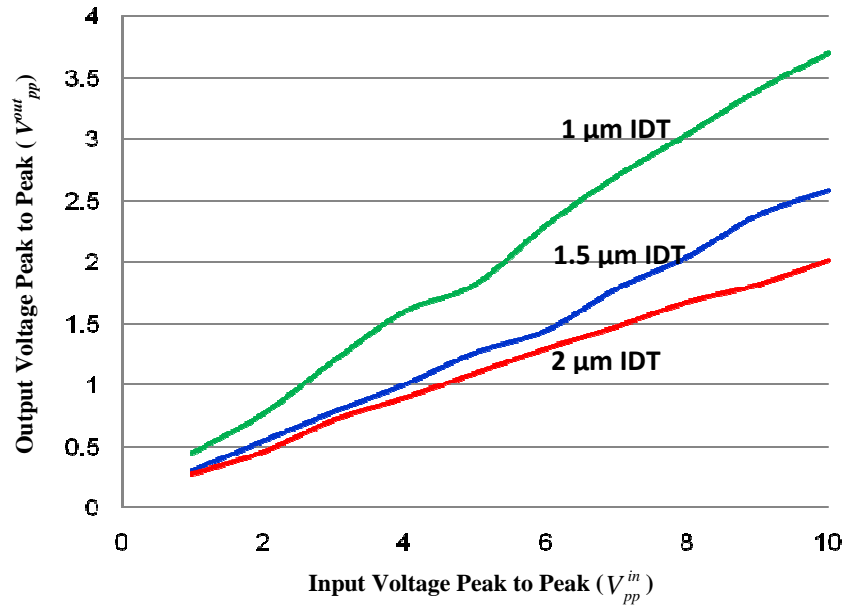
Figure 4.13: Output voltage peak to peak versus input voltage peak to peak (V_{pp}^{out} vs V_{pp}^{in}) in different IDT electrode dimensions of the SAW sensor

As shown in Figure 4.13, the 1 µm IDT electrode SAW sensor showed the highest output peak to peak and the 2 µm IDT SAW was the lowest output as expected based on the theory.

4.2.4 Sensor Calibration

The operational frequency of the SAW sensor measured by the network analyzer is shown in Figure 4.14.
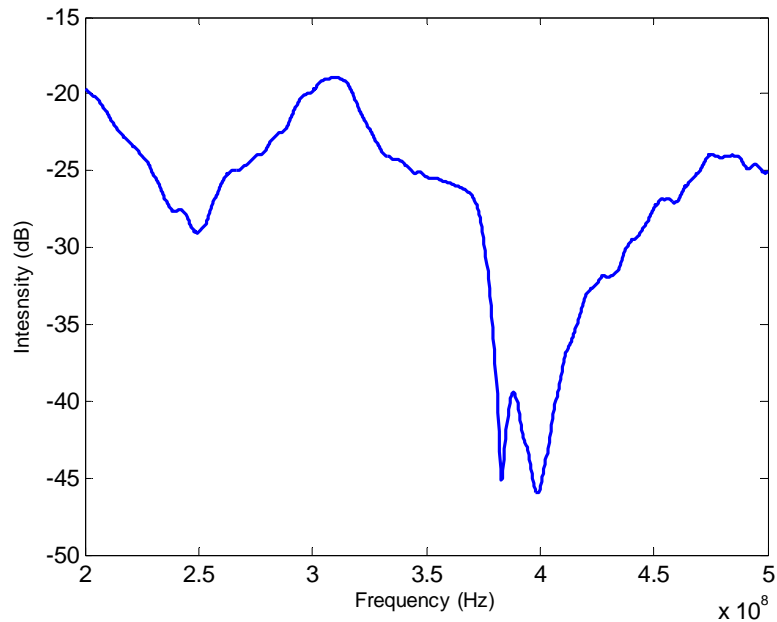
Figure 4.14: Operational frequency of the SAW sensor (S_{11}) (Low peak represents the resonant frequency)

The resonant frequency of the SAW sensor corresponds to the low peak in the S_{11} parameter analysis at the network analyzer. As shown in Figure 4.14, there were two major peaks around 385 MHz and 401 MHz. The 401 MHz peak was the operational frequency for which the device was designed, but the 385 MHz peak might be due to the acoustic wave dispersion because the IDT was not located over the ZnO piezoelectric substrate. Hence, it was acceptable to use either peaks to calibrate the device.

The detection limit and sensitivity of the SAW sensor were studied by loading 10 µl of deionized (DI) water on the sensor. The mass sensitivity of the SAW sensor is defined in equation (14).

$$S_m^v = \lim_{\Delta m \to 0} \frac{1}{\Delta m}\left(\frac{\Delta v}{v_0}\right) = \lim_{\Delta m \to 0} \frac{1}{\Delta m}\left(\frac{\Delta f}{f_0}\right) \qquad (14)$$

where S_m^v is the mass sensitivity of the SAW sensor, v_0 is the initial SAW velocity before mass loading, Δm is the amount of the mass loading, Δv is the SAW velocity change due to the mass loading, Δf is the resonant frequency shift, and f_0 is the operational frequency. Therefore, at a given operational frequency the sensitivity of the sensor is equal to the frequency shift divided by the additional mass loading. In the device calibration, Δm was 10 µg.

The resonant frequency shift produced by water loading is shown in Figure 4.15.
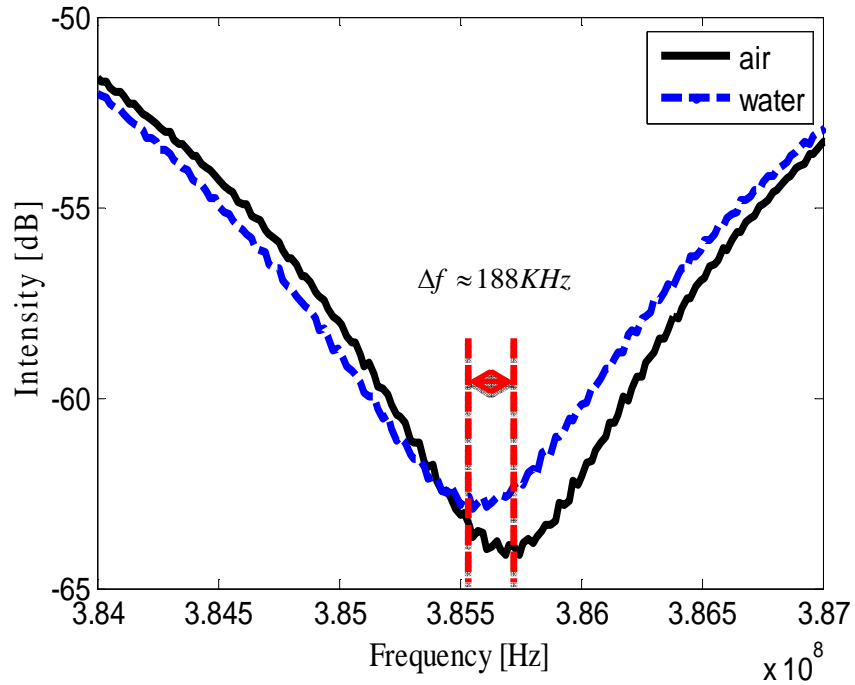
Figure 4.15: Resonant frequency shift due to 10 µl DI water loading

For the calibration purposes, the 385 MHz peak was used since the Q factor was better than that for 401 MHz peak. As shown in Figure 4.15, the resonant frequency of the SAW sensor was negatively shifted about 188 KHz. Therefore, the sensitivity would be approximately $1.88 \times 10^{10} \, Hz/g$ based on the water loading characterization work. The resolution of the network analyzer was 0.1 Hz. Thus, the minimum detectable mass, which was calculated by the resolution of the equipment divided by the sensitivity of the sensor, was approximately $5.3 \times 10^{-12} \, g$.

Before the bacterial growth experiment, an 10 µl overnight suspension culture of *E. coli* was loaded on the SAW sensor. Figure 4.16 shows the frequency response upon the bacterial solution loading.
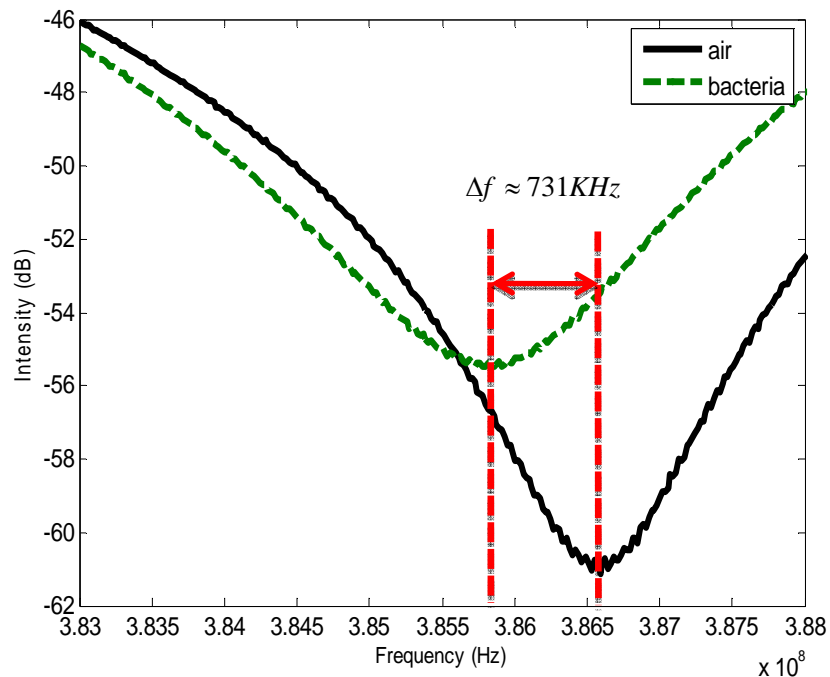
Figure 4.16: Resonant frequency shift due to 10 µl *E. coli* bacteria loading

As shown in Figure 4.16, the resonant frequency shift produced by bacterial solution loading was about 731 KHz, which was a significantly higher resonant frequency change than produced by loading 10 µl of DI water. This was because of the viscosity difference between two solutions.

Based on the perturbation theory [70], a liquid loading modifies the propagation constant of the acoustic wave. As a result, the acoustic wave penetrates to the liquid side causing the loss of the signal. The depth of the acoustic wave penetration is in equation (15)[71].

$$\delta = \sqrt{\frac{2\eta}{\rho\omega}} \qquad (15)$$

where δ is the depth of the acoustic wave penetration, η is the viscosity of the solution, ρ is the solution density, and ω is the propagation frequency. Based on the penetration depth relation with the viscosity, the acoustic wave would be more attenuated in contact with a high viscosity liquid. Thus, the loading of the bacterial solution on the SAW sensor resulted in a higher negative frequency change than that produced by loading DI water.

4.3 *In vitro E. coli* Biofilm Growth Experiments

4.3.1 Bacterial Growth Media

The biofilm SAW sensor was tested in two different types of growth media, which were Lysogeny Broth (LB) and 10% Fetal Bovine Serum (FBS) diluted by Dulbecco/Vogt modified Eagle's minimal essential medium (DMEM).

The LB has become an industrial standard for *E. coli*. cultivation far back in 1950's and it is the most common media used in molecular microbiology applications. LB media is mainly composed of yeast, NaCl, and amino acids. Amino acids, such as tryptophan, are the source for the protein synthesis need for bacterial growth. Yeast provides certain vitamins and trace elements, such as magnesium and nitrogen. NaCl produces an osmotic pressure balance of the bacteria in the media. In this wrok, LB media was used as an optimized environment for *E. coli* growth to investigate the SAW sensor response.

In addition to the LB media, the SAW sensor was also studied in 10% FBS as an approximated *in vivo* environment to see the sensor performance in an animal serum. FBS is derived from blood drawn from a bovine fetus and blood cells are separated by centrifugation or natural coagulation by fibrinogen. The globular protein, Bovine Serum Albumin (BSA), is the main component of the FBS together with many other proteins. Due to the rich variety of proteins and similarities to an *in vivo* environment provided by FBS, it is the most widely used growth media for mammalian cell culture. The

SAW sensor was tested in 10% FBS as a simulated *in vivo* condition to inspect the device response for future implantable applications.

4.3.2 Sensor Reusability

One of the key requirements for the implantable application is the sensor reliability, so that a patient does not have to undergo revisional surgery to replace the device. For the reliability investigation of the SAW sensor, the sensor was tested at least three times consecutively and the device output was analyzed. However, the cleaning of the device was very critical for the continuous use of the SAW sensor in multiple experiments because of the strong biofilm adhesion to the sensor surface. The clean surface of the SAW sensor was also important in keeping the same level of sensitivity since the initial mass loading on the sensor would cause a loss in sensor sensitivity. Hence, an effective cleaning method for biofilm removal from the SAW sensor had to be developed.

At first, the biofilm-contaminated SAW sensor, passivated by the 45 nm ALD Al_2O_3 film, was placed into acetone solution which is widely used to clean polymers in biological and microfabrication processes. The biofilm on the surface of the sensor was inspected using optical microscope after acetone cleaning as shown in Figure 4.17.
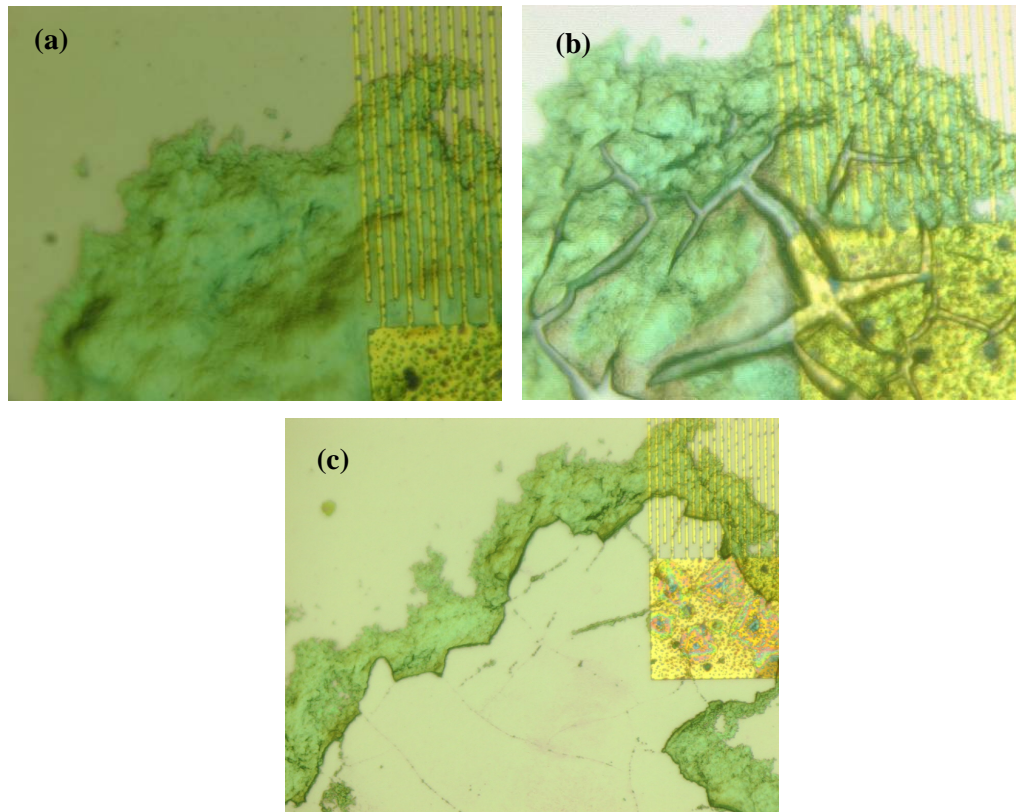
Figure 4.17: Cleaning of device by acetone, (a) Device cleaned with DI water after a biofilm experiment (biofilm remained on the sensor), (b) Device cleaned by ultrasonication in acetone (biofilm was broken, but still adherent), (c) Device cleaned with acetone at 100 °C hotplate for three hours (majority of the biofilm was cleaned, but it was not clean enough for subsequent experiments)

The surface of a SAW sensor cleaned by DI water is shown in Figure 4.17(a). The biofilm adhered so strongly that DI water cleaning did not remove it. Then, cleaning of the sensor was attempted using ultrasonication in acetone for 30 minutes as shown the images in Figure 4.17(b). As an alternative method, the device was heated at 100 °C in an acetone solution for three hours since the biofilm was still adherent after acetone cleaning at room

temperature. To prevent the evaporation of the acetone in the heating acetone cleaning process, the device was placed in a 500 mL beaker containing 300 mL acetone and sealed the top with paraffin film. After three hours of heated acetone cleaning, the majority of the biofilm wa removed. However, biofilm residues were observed by optical microscopy as shown in Figure 4.17(c). Even if the device was cleaned for longer than three hours using the heated acetone cleaning method, the surface of the SAW sensor was not cleaned sufficient for the next experiment.

Bleach is well known as an excellent choice for cleaning of organic materials cleaning. The biofilm-covered SAW sensor was attempted to be cleaned using a 15 times water diluted bleach solution. The biofilm on the surface of the SAW sensor shown in Figure 4.18(a) was placed in the diluted bleach solution for 2 minutes. After bleach cleaning, the surface of the device was extremely clean as shown in Figure 4.18(b), so the device could be used in the next biofilm growth experiment.
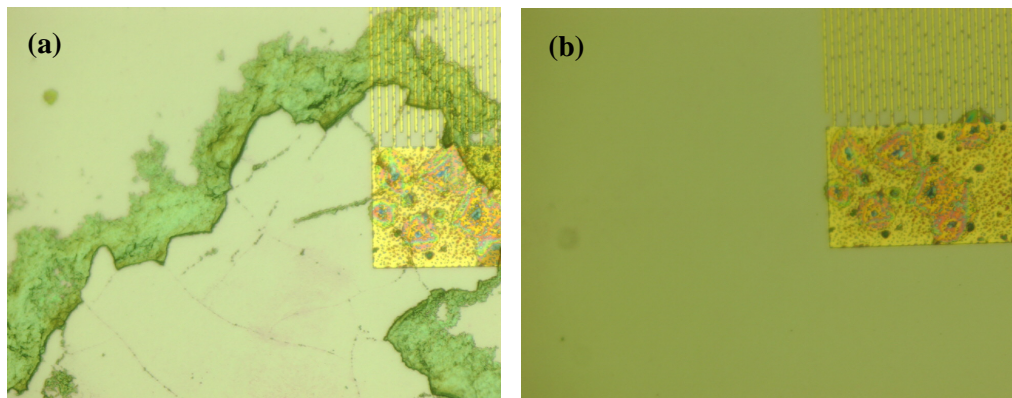
Figure 4.18: (a) before and (b) after 15 times diluted bleach cleaning for two minutes

Before the next biofilm growth experiment, the cleaned device was recalibrated by monitoring the resonant frequency shift due to the DI water loading. Results showed almost the same sensitivity as compared with the initial device. Then, the recalibrated SAW sensor shown the optical image of the sensor in Figure 4.19(a) was tested in a second biofilm growth experiment using the same procedure. However, after the second experiment with the bleach cleaned sensor, the ZnO film was damaged by the bacterial growth media, as shown in Figure 4.19(b). Due to the ZnO film damage, the output of the SAW sensor was not observed in the second biofilm growth experiment.
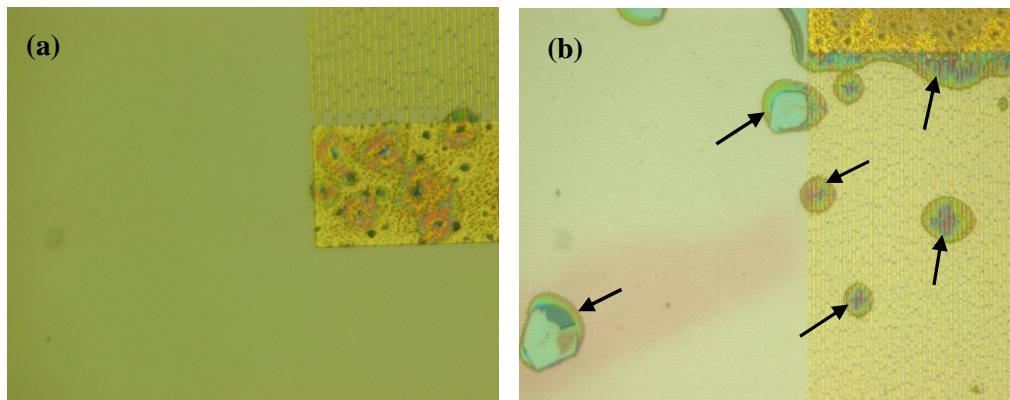
Figure 4.19: (a) Device surface after bleach cleaning, (b) ZnO damage after the second biofilm growth experiment in the bleach cleaned device (arrows indicate ZnO damage areas)

The ZnO damage after the second test using the bleach-cleaned chip was shown consistently after many attempts. The ZnO damage can be due to the fact that the bleach is not a neutral pH solution. The bleach can cause

chemical decomposition of the Al_2O_3 thin film deposited by ALD during the cleaning procedure, resulting ZnO damage.

Oxygen (O_2) plasma was then applied for cleaning of the biofilm from the SAW sensor. O_2 plasma removes impurities and contaminants from surfaces through the use of energetic plasma created from oxygen gas. The vacuum ultraviolet (VUV) energy is very effective for the breaking most organic bond of surface contaminants. This helps to break apart high molecular weight contaminants. A second cleaning action is carried out by the oxygen species created in the plasma (O_2^+, O_2^-, O_3, O, O^+, O^-, ionized ozone, metastably-excited oxygen, and free electrons). These species react with organic contaminants to form H_2O, CO, CO_2, and lower molecular weight hydrocarbons. These compounds have relatively high vapor pressures and are evacuated from the chamber during processing. The resulting surface is ultra-clean.

With those advantages of O_2 plasma cleaning, the ALD Al_2O_3 passivated SAW sensor can be effectively cleaned, as shown in Figure 4.20.
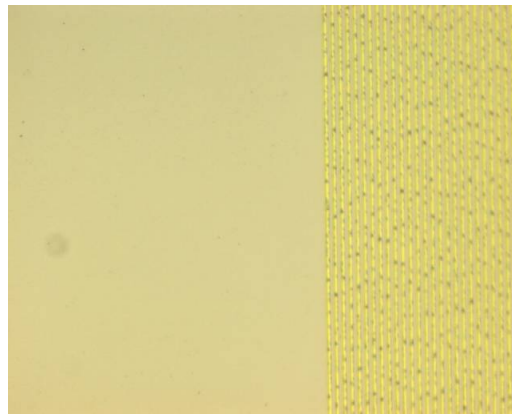
Figure 4.20: Optical image of the O_2 plasma cleaned SAW sensor (20X)

The O_2 plasma cleaned device was characterized by DI water loading, and the sensitivity of the sensor was maintained over three consecutive experiments. The detection limit results after each biofilm formation experiment are summarized in table 5.

	Before biofilm experiment	After 1st biofilm growth experiment	After 2nd biofilm growth experiment	After 3rd biofilm growth experiment
Detection limit	49.4 pg	51.9 pg	53.4 pg	55.7 pg

Table 5: Summary of the SAW sensor detection limit in sequential biofilm growth experiments

The detection limit of the sensor became slightly worse with the sequential biofilm growth experiments (table 5), but was still three orders more sensitive than the biofilm loading mass, which was on the order of hundreds of micro grams. The key product of these experimental results was that the ZnO did not show any damage after consecutive biofilm growth experiments as shown in Figure 4.21.
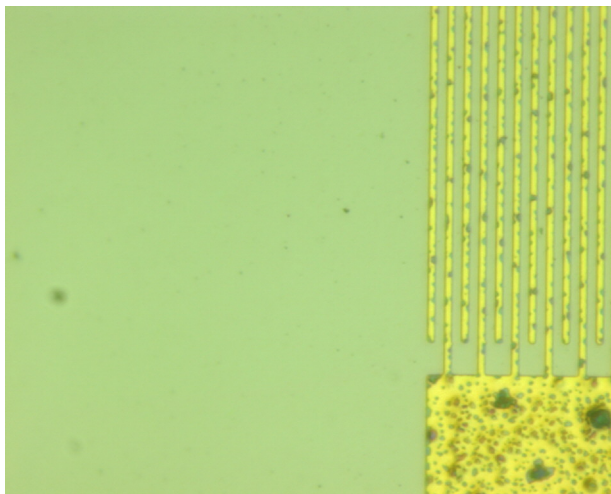
Figure 4.21: The ALD Al$_2$O$_3$ passivated SAW sensor surface after three consecutive biofilm experiments using O$_2$ plasma cleaning between uses

Based on this result, O$_2$ plasma cleaning was selected over acetone and bleach cleaning since it allowed the SAW sensor to be used multiple times in the biofilm growth experiments without ZnO film damage.

4.3.3 The SAW Sensor Biofilm Growth in LB media

To prepare bacteria for the SAW sensor biofilm growth test, a 20 μl frozen culture of Escherichia coli (*E. coli*) W3110 was put into 5 ml of LB media in a cell culture tube. Then, the bacteria were cultured overnight in the 200 rpm shake incubator at 37 °C for 16 hours. The optical density (OD$_{600}$) was measured after the overnight culture growth, and the OD was 4.20 - 4.50. 1 ml of the overnight cultured bacteria was placed in the bacterial growth well

in the device package and was diluted 20 times by adding LB media to achieve the initial bacterial concentration over the SAW sensor to be 0.21 - 0.23. Then, the device package was held at 37 °C and covered by paraffin film to prevent the bacterial solution evaporation during the biofilm growth experiment. The final testing setup is shown in Figure 4.22.
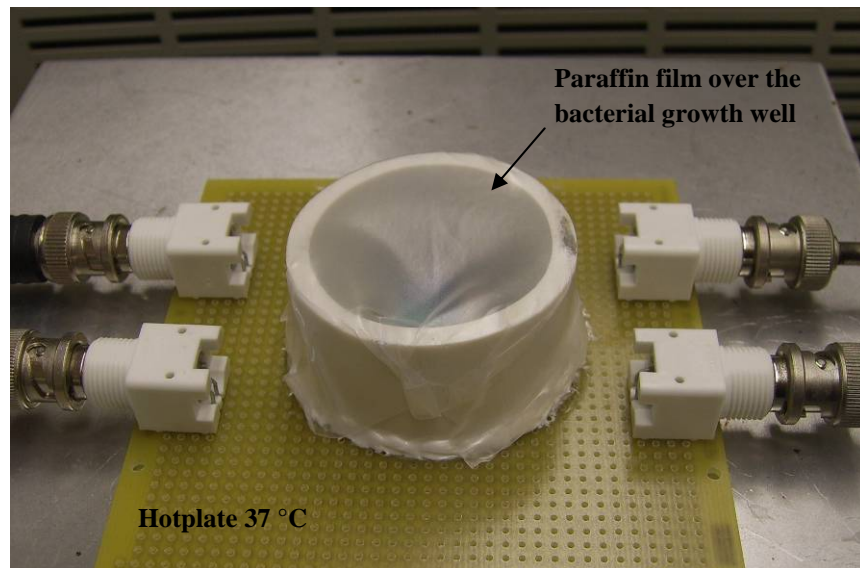
Figure 4.22: Testing setup for biofilm growth experiment (The bacterial growth well is sealed by paraffin film in the biofilm growth experiment. Also the whole package is covered by a polystyrene container during the experiment.)

To read out the resonant frequency change during the biofilm growth, the package was connected with the network analyzer, and the resonant frequency was saved every minute to the computer by using GPIB communication.

Two types of SAW sensors with different IDT dimension were tested in biofilm growth in LB media. Theoretically, the smaller dimension of IDT has a higher sensitivity than the wide electrode of IDT, since the narrow electrode

IDT allows more energy transmission due to high energy insertion efficiency[58].

The resonant frequency shift results of the SAW sensor over the biofilm

growth are shown in Figure 4.23.
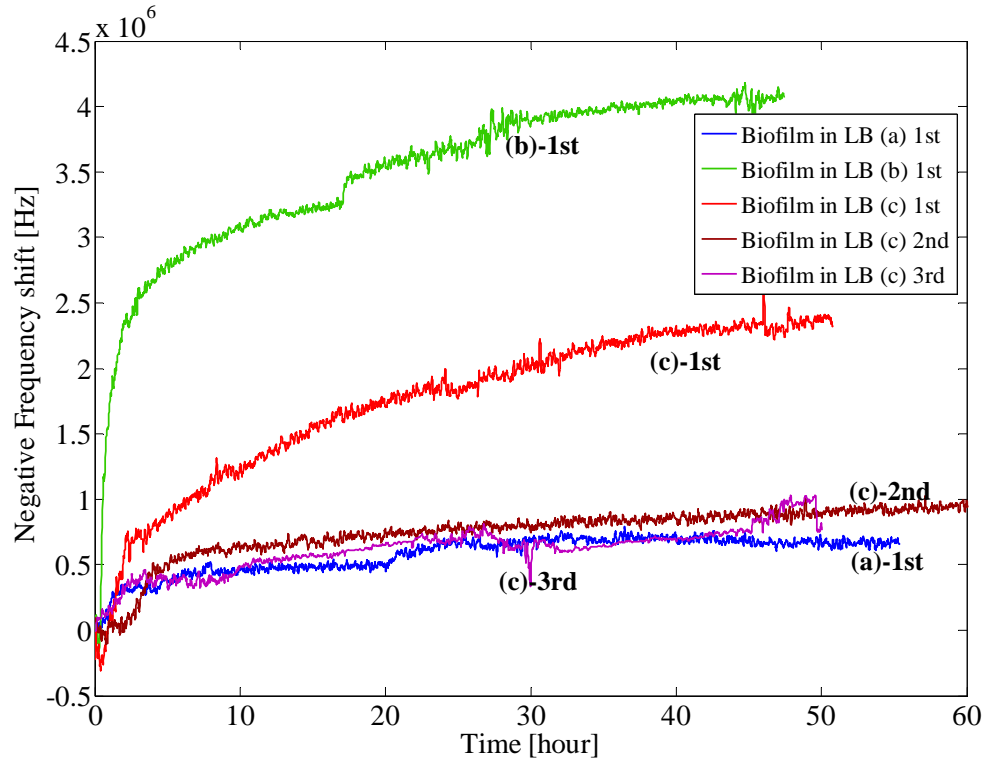
Figure 4.23: Resonant frequency shift results of the SAW sensor in LB media biofilm growth experiment using ((a) - 1.5 µm IDT, (b) – 2 µm IDT, and (c) – 2 µm IDT indicate different device with same fabrication process. 1st, 2nd, and 3rd indicate the order of the consecutive biofilm formation experiment.)

The negative frequency shift of the sensor was defined as the difference

between the initial resonant frequency and the measured frequency in the test.

The negative frequency of the SAW sensor was proportional to the mass

loading, which was caused by the biofilm growth in this case, so the negative

frequency shift corresponded to the bacterial growth state.

The data in Figure 4.23 was shown for the 2 μm IDT SAW sensor excepting the blue curve, which was obtained with a 1.5 μm IDT SAW sensor. The blue, green, and red curves represented the new SAW sensor frequency shift over the first biofilm growth experiment with that sensor. The brown and black curves corresponded to the second and third biofilm growth experiments using the same SAW sensor as the red curve following oxygen plasma cleaning between uses.

As shown in the results, the output of the SAW sensor showed a rapid change at the beginning of the experiment, and reached a steady state about 20 hours later. To investigate the growth rate in each experiment, the linear growth rate, which was the mass increase per hour at the beginning of the experiment as shown in equation (16), was calculated and summarized in table 6, based on the SAW sensor detection limit and equipment resolution.

$$\text{Linear growth rate} \, [\mu g \, / \, hr] = \frac{[\text{frequency shift at 20 hours} \times \text{detection limit}]}{[\text{equipment resolution} \times 20 \, \text{hours}]}$$

(16)

Data	Green	Red	Brown	Black	Blue
Linear growth rate	86.8 μg/hr	49.6 μg/hr	17.4 μg/hr	14.9 μg/hr	11.2 μg/hr

Table 6: Linear growth rate after 20 hours in the biofilm growth

As shown in table 6, the growth rates were different from each other even if the device dimensions were the same. Bacterial growth rate was generally affected by temperature, growth media composition, pH, and mechanical movement of the setup during static biofilm growth. In the testing setup, the temperature was maintained at 37°C using a hotplate, and the device package was covered by a polystyrene container to thermally isolate the setup from external heat exposure or absorption. The initial bacterial concentration was also always the same concentration, and the same LB media was also used between experiments. Based on these controlled conditions, it was reasonable to set a hypothesis that the variance of the output SAW sensor might be due to the natural bacterial growth variance in LB media since the sensor did not show much variance in the DI water calibration work performed after each biofilm growth experiment.

To investigate the variance of bacterial biofilm growth in LB media, six 45 nm Al_2O_3 passivated ZnO test chips were prepared in a 6 well plate, which was filled with the same OD_{600} concentration (0.21-0.23) of *E. coli* solution. The 6 well plate was placed on the 37°C hotplate and covered by the polystyrene container as in the biofilm growth experiments. Two days later, the biofilm thickness was measured by an optical microscope using Z-axis measurement technique in 30 - 40 locations per chip. The average and standard deviations of the biofilm thickness were calculated as shown in Figure 4.24.
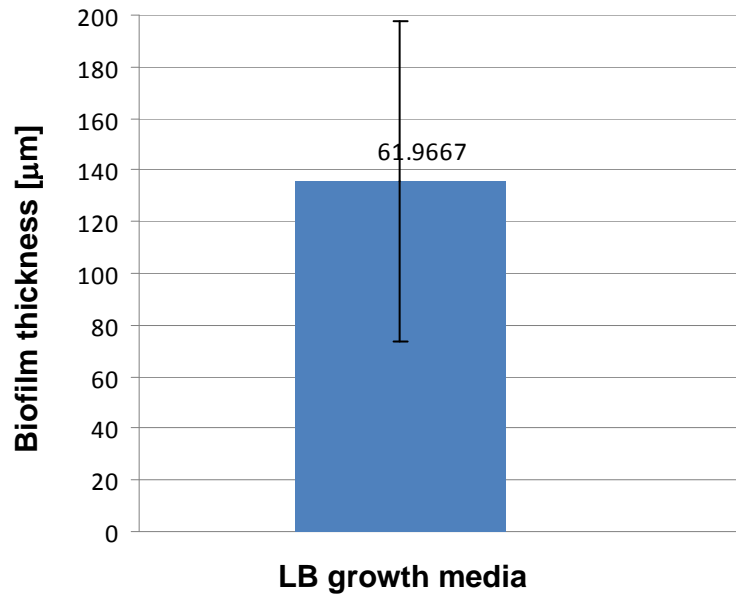
Figure 4.24: Average biofilm thickness and standard deviation measured by an optical microscope in LB media (average thickness: 135 µm, standard devication: 61.97 µm)

As shown in Figure 4.24, the average biofilm thickness in LB media was approximately 135 μm, and the standard deviation was about 62 μm, which was 46 % of the average biofilm thickness. The optical images of the biofilm grown on the surface of the SAW sensor were also inspected by the optical microscope as shown in Figure 4.25.
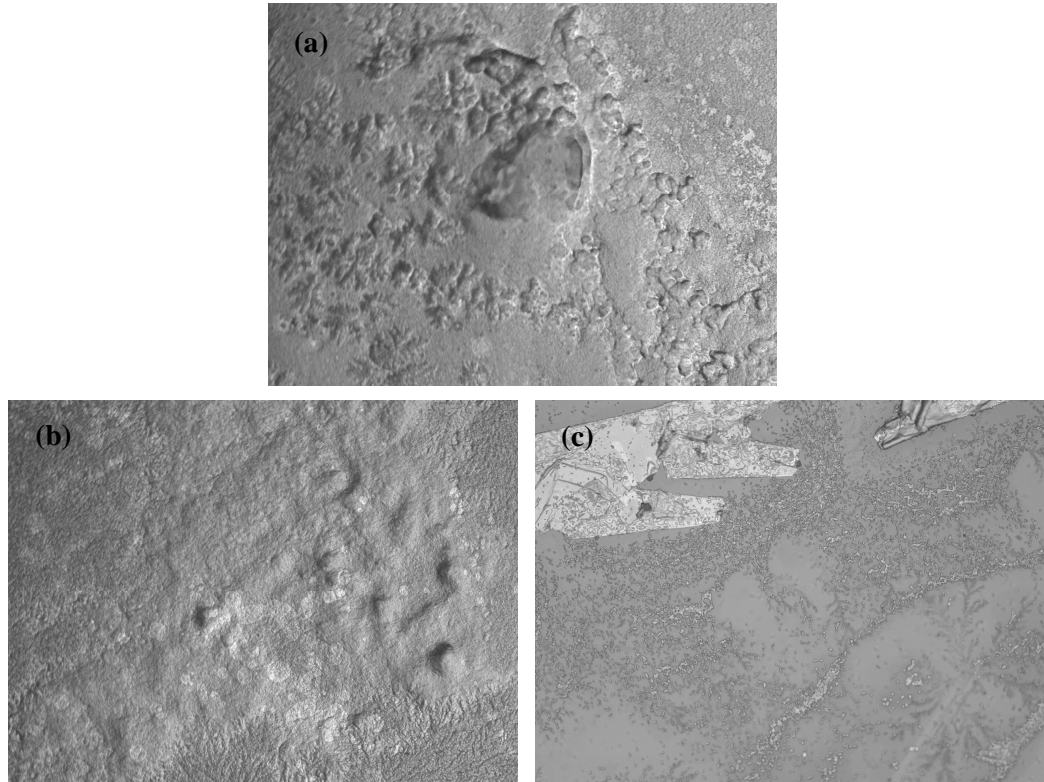
Figure 4.25: Optical images of the biofilm formed on the SAW sensor in LB media with the thickness of (a) 184 μm, (b) 133 μm, (c) 30 μm

Thus, if the bacterial biofilm was grown thicker over the SAW sensor as shown in Figure 4.25(a), the overall resonant frequency shift of the sensor would be higher than that of the others in Figure 4.25(b) and (c), since the resonant frequency shift is proportional to the mass loading on the sensor.

These experimental results suggest the resonant frequency shift variance of the output at the SAW sensor in LB growth media (Figure 4.23) can be due to the nature of the non-uniform biofilm formation.

4.3.4 The SAW Sensor Biofilm Growth in 10% FBS

The SAW sensor was also tested in animal serum, which was Fetal Bovine Serum (FBS), to investigate the device performance in a simulated *in vivo* environment. The 10% FBS diluted by DMEM was filled in the bacteria growth well of the package over the SAW sensor with the cultured *E. coli,* which was prepared along with the same procedures as in LB media experiments. The initial concentration of the bacterial suspension was also 0.21 - 0.23 as in LB media biofilm growth experiment.

The sensor was tested three times sequentially to prove the reliability of the SAW sensor in monitoring biofilm growth. After a biofilm growth experiment, the 45 nm ALD Al_2O_3 passivated SAW sensor was cleaned using O_2 plasma for 30 s. The negative resonant frequency shift results of the SAW sensor in 10% FBS are shown in Figure 4.26.
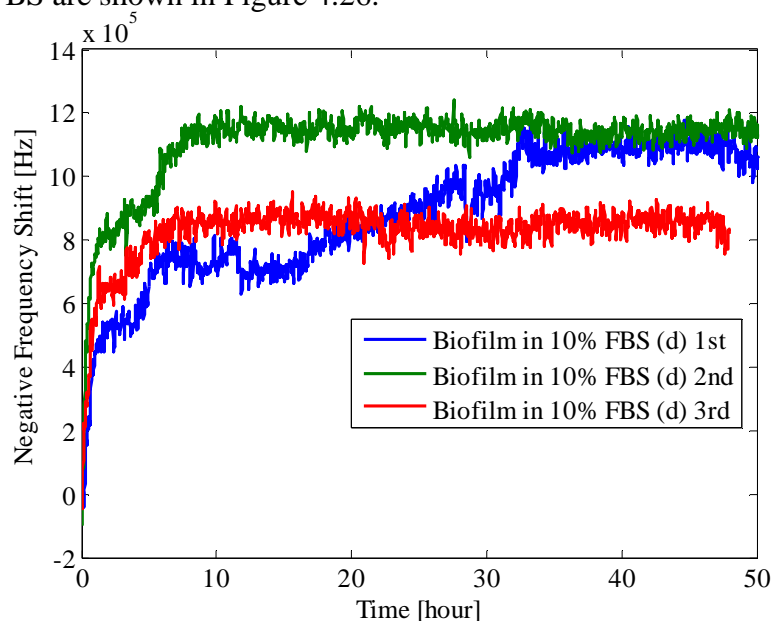
Figure 4.26: Resonant frequency shift of the SAW sensor in 10% FBS ((d) indicates a different SAW sensor with the same dimension and fabrication process)

76

As shown in Figure 4.26, the resonant frequency shifts of one SAW sensor in 10% FBS over all three experiments more closely corresponded with each other than the results from LB media biofilm formation experiments. The three overall resonant frequency shifts at the stationary phase were about 1 MHz, and showed only 0.2 MHz difference between each other which is less variations as compared to the 3 MHz frequency shift difference in LB media. Since the 10% FBS is not an optimized growth media for bacterial growth, the biofilm growth could be suppressed due to the nutrient deficiency or composition difference from LB media. Thus, any minor environmental changes, such as temperature and pH, may not make a big difference in the bacterial growth.

The biofilm growth variance in 10% FBS was also performed using six test chips with the same preparation procedures as in LB media. The biofilm thickness measured by the optical microscope z-axis displacement technique with the LB media results is shown in Figure 4.27.
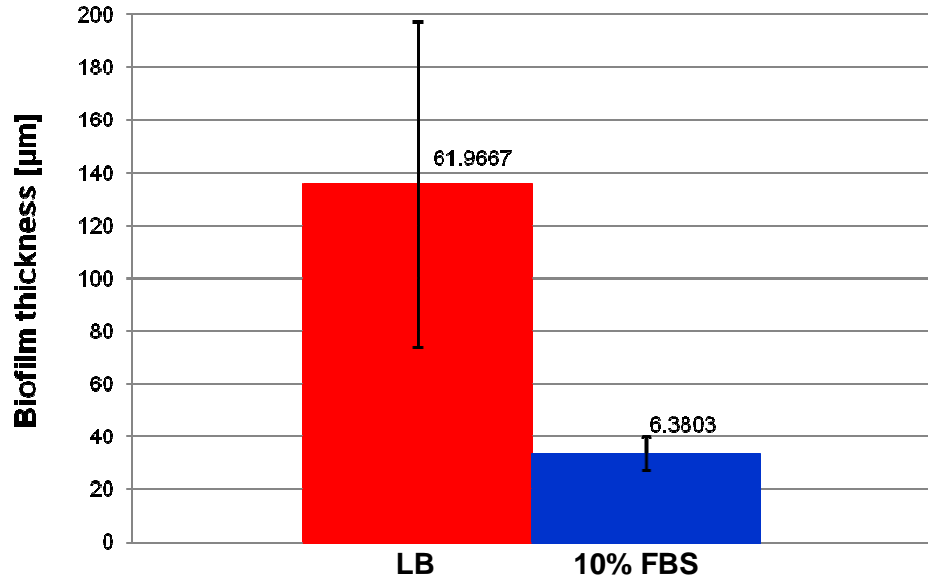
Figure 4.27: Average biofilm thickness and standard deviation measured by an optical microscope in LB and 10% FBS

As shown in Figure 4.27, the average biofilm thickness in 10% FBS was about 32 µm and standard deviation was about 6.4 µm, which is less variation than in LB results. Based on this experimental result, the low variation of the resonant frequency shift of the SAW sensor in 10% FBS could be due to the uniform biofilm growth in 10% FBS. The biofilm images from select locations on the test device are shown in Figure 4.28.
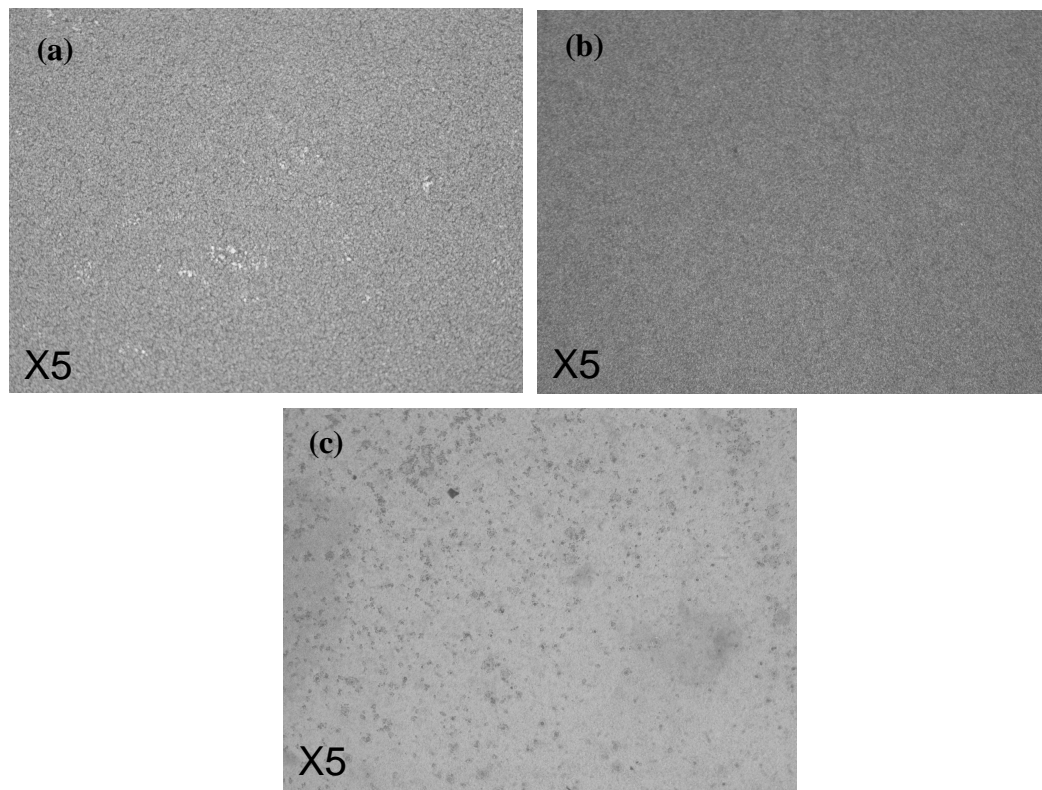
Figure 4.28: Three different biofilm growth optical images in the same device from 10% FBS biofilm growth experiments with the thickness (a) 37 μm, (b) 50 μm, (c) 24 μm

Since the biofilm growth in 10% FBS was uniform as shown in Figure 4.28, the resonant frequency shift of the SAW sensor in the media (in Figure 4.26) was also less variable between biofilm experiments in 10% FBS than in LB media (in Figure 4.23) based on the mass loading and proportional resonant frequency shift in the SAW sensor.

5. Discussion

5.1 Passivation of the SAW sensor

Based on the passivation modeling calculation results, Al_2O_3 and Si_3N_4 were chosen as a passivation film in the SAW sensor. The minimum thicknesses of Al_2O_3 and Si_3N_4 films were determined based on the ZnO surface inspection using optical microscopy after two days in bacterial growth media. Different thicknesses of a passivation film were deposited on the SAW sensor and the surface of the sensor was inspected for ZnO damage by optical microscopy. Based on this preliminary work, the thicknesses of Al_2O_3 and Si_3N_4 films required for the passivation of the ZnO were at least 45 nm and 40 nm respectively.

The 40 nm Si_3N_4 deposited by PECVD cannot protect ZnO in the bacterial biofilm growth experiments (in Figure 4.8 and 4.9). This result of the Si_3N_4 passivated SAW sensor can be because of the non-uniform and less conformal film deposition in the PECVD.

Al_2O_3 thin film was deposited 45 nm over the SAW sensor using ALD, E-beam evaporation, and RF-sputtering to investigate the fabrication process dependence in the passivation film performance. As a result of the bacterial solution exposure of the SAW sensor for two days, Al_2O_3 deposited by ALD can protect ZnO, but Al_2O_3 using E-beam evaporation and RF-sputtering did not prevent ZnO damage. Since the ALD has highly dense and conformal thin film deposition capabilities, the ALD Al_2O_3 film can passivate the ZnO over more than one week of exposure to a bacterial solution in

consecutive biofilm formation experiments. Therefore, ALD is the key fabrication process for the passivation of the SAW sensor using a 45 nm Al_2O_3 thin film.

5.2 Correlation with Natural Bacteria Growth Model

The mathematical modeling of the natural bacterial growth has been studied by many other scientists[72]. Models are used to describe the behavior of microorganisms under different physical or chemical conditions such as temperature, pH, and flow rate. These models allow for the prediction of microbial population and the detection of critical parts of production and distribution processes. The key characteristics of the bacterial growth model are the initial exponential growth and stationary stage. In nature, low populations of bacteria start to grow exponentially at the beginning of the growth, and then reach a stationary stage due to the high population density and limited nutrient supply[73].

A mathematical bacterial growth model was used to analyze of the resonant frequency shift results from the SAW sensor. The Gompertz bacterial growth model[66] was used to compare with the SAW sensor results due to the simplicity and mathematically normalized biological growth parameters in the equation (17).

$$y = ae^{[-e^{(b-ct)}]} \qquad (17)$$

where y is the population of the bacteria, t is time, a, b, and c are mathematical growth parameters depending on the bacterial growth environment. The mathematical parameters can be determined by the biological experiments or mathematical approximations. Here the growth parameters were chosen to normalize the growth population so that the SAW sensor results could be compared directly with the model. Based on the mathematical normalization calculation[66], all of the parameters became one.

Since the negative frequency shift of the SAW sensor was related to additional mass loading due to the biofilm growth, it was possible to compare bacterial population directly to the negative resonant frequency shift. The resonant frequency shift of the SAW sensor was normalized with respect to the final frequency shift. By normalizing the response of the SAW sensor, which represented the relative growth, the negative resonant frequency shift became unitless data so that the direct comparison between the model and SAW sensor results could be acceptable. As a result, the y axis of the normalized frequency response in the SAW sensor represented the relative bacterial population growth rate and also the stationary stage became one. The normalized SAW sensor results in LB media and the mathematical model were plotted together in Figure 5.1.
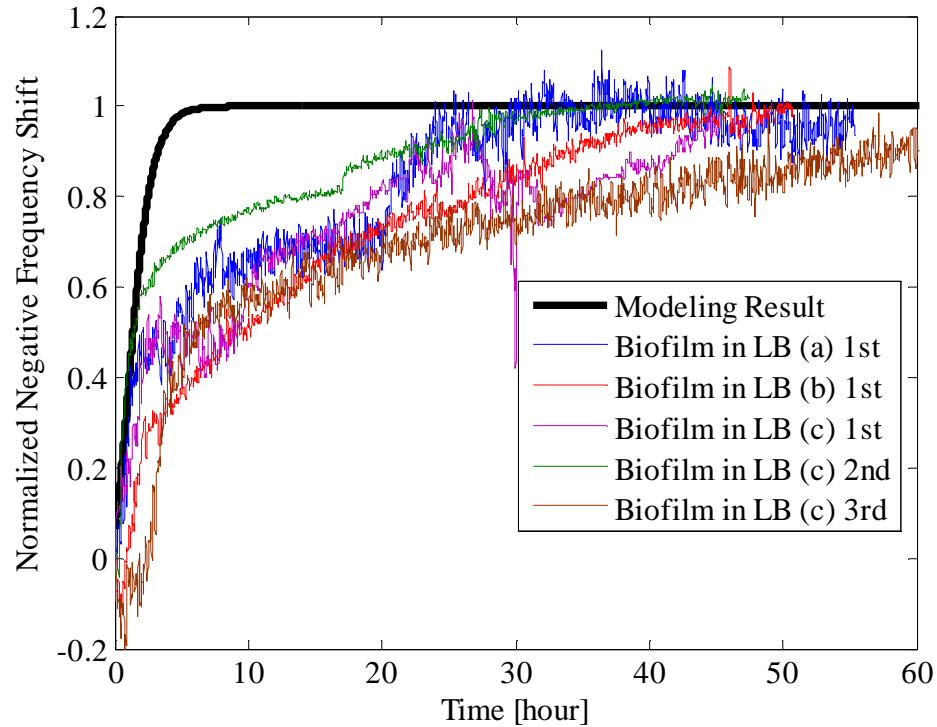
Figure 5.1: Normalized resonant frequency shift result in LB with the Gompertz bacterial growth curve, ((a), (b), (c) indicate different devices with the same dimension and fabrication processes, 1st, 2nd, and 3rd indicate the order of the consecutive biofilm growth experiment.)

As shown in Figure 5.1, the SAW sensor results from LB media biofilm formation experiments followed the exponential growth of the model at the beginning, but it reached stationary phase about 20 hours later than the model. This difference between the model and experimental results can be due to the static bacterial growth in the SAW sensor biofilm formation experiment, which did not supply fresh nutrients continuously during the experiment. In addition, the mathematical parameters in the model were normalized rather than determined by based on biological experimental approaches. However, all normalized frequency shift results in the SAW sensor were

closely corresponding to each other, since the maximum difference in the stationary

phase frequency shift was only about 10%.

The normalized 10% FBS resonant frequency shift results were compared with the

same mathematical model in Figure 5.2.
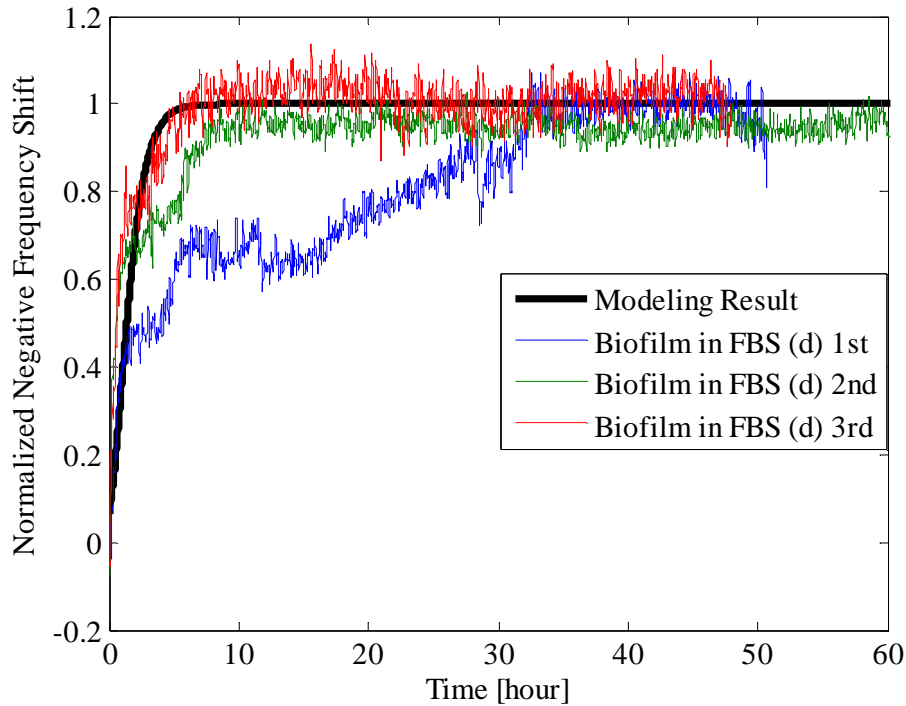
Figure 5.2: Normalized resonant frequency shift result in 10% FBS with the Gompertz bacterial growth curve ((d) indicates a different device. 1st, 2nd, and 3rd mean the order of the consecutive experiments.)

The normalized 10% FBS results more closely followed the model as compared to

the SAW sensor results from LB media biofilm formation experiments. Except for the

first experimental result in 10% FBS, the others followed the exponential growth rate

at the beginning and reached to the stationary stage about 10 hours, matching the

modeling curve. This result can be due to the similarities to *in vivo* environment from the 10% FBS composition. This more corresponding results in 10% FBS validate the SAW sensor for the future *in vivo* biofilm detection.

6. Conclusions

This thesis work successfully demonstrated for the first time the design, fabrication, and testing of the bacterial biofilm growth monitoring using the SAW sensor. The sensor was fabricated using a c-axis oriented high quality ZnO deposited by PLD. The confirmed c-axis orientation by XRD ZnO thin film allowed for generating Love mode SAW, which was the key requirement for the SAW biosensor application. For the passivation of the ZnO film to avoid damage resulting from long term growth media contact, 40 nm PECVD Si_3N_4 and 45 nm Al_2O_3 by ALD or E-beam evaporation or RF-sputtering were tested in the bacterial solution for two days. As a result of the experiments, 45 nm thickness Al_2O_3 film deposited by ALD was only able to passivate ZnO layer due to the high dense and conformal film deposition capabilities of the ALD. Moreover, the SAW sensor can be used again based on the oxygen plasma biofilm cleaning after multiple biofilm formation tests. Based on the novel ALD Al_2O_3 film passivation and unique O_2 plasma cleaning procedure, the SAW sensor can be used in multiple biofilm growth experiments without losing sensitivity. The detection limit of the SAW sensor studied by 10 µl DI water loading was approximately 5.3 pg.

The resonant frequency shift results in LB media and in 10% FBS followed the initial exponential growth and subsequent stationary phase that are the key characteristics of the mathematical bacterial growth model. Normalized resonant frequency shift results of the SAW sensor representing the relative growth in LB media and in 10% FBS were compared to the Gompertz bacterial growth curve due to the simplicity and mathematically normalized biological growth parameters of the equation. The normalized 10% FBS results more closely followed the model as compared to the SAW sensor results from LB media biofilm formation experiments.

These repeatable results that correspond well with the natural bacterial growth model measured at the output of the SAW sensor validate the novel application of the SAW sensor for bacterial biofilm growth monitoring and future implantable applications based on the more correlated results in 10% FBS.

7. Future Work

To develop an implantable biofilm sensor, it is required to have a wireless read out method at the sensor output. Since the SAW sensor does not need to have a DC input source, it is possible to remove electronics components to convert electrical signal from AC to DC. As a result, the interface between a RF wireless signal and SAW sensor is more compatible than in other sensing methods. One possible method to develop the wireless biofilm SAW sensor would be using RF-inductive coupling[74].

Another future direction is the functionalization of the SAW sensor to provide selectivity[75]. However, this sensor selectivity work presents a significant challenge

considering the future implantable applications. Upon placement of foreign material *in vivo*, the immune system and self defense mechanism start to attack the heterogeneous material and finally encapsulate it, in a process called biofouling[76-77]. As a result, without overcoming the biofouling challenges[78] , any functionalized SAW sensor cannot be applied for implantable applications. This is a significant challenge to be overcome in development of the implantable biosensor.

In addition, the effect of human tissue on SAW attenuation should be investigated. When an electromagnetic wave meets human tissue, the amplitude and frequency of the signal are attenuated due to the dielectric constant and density difference provided by skin, blood, and bone[79]. This attenuation effect may require changing the device dimensions to increase the sensitivity. The sensitivity of the SAW sensor can be improved by depositing ZnO thicker than 400 nm.

Finally, system modeling would aid future sensor system development. The final implantable biofilm monitoring system is composed of the SAW sensor, RF wireless communication, the human body interface, and the immune defense system. These components are not simply separated from each other, but interact very closely. Therefore, the modeling of the entire system is critical to study what factors should be considered in integrating the system.

Appendix A

Network analyzer data save program (S$_{11}$)

```c
/*
 *  Include the WINDOWS.H and DECL-32.H files. The standard Windows
 *  header file, WINDOWS.H, contains definitions used by DECL-32.H and
 *  DECL-32.H contains prototypes for the GPIB routines and constants.
 */

#include "stdafx.h"
#include <stdio.h>
#include <time.h>

#define ARRAYSIZE 100              // Size of read buffer

int  Dev;                          // Device handle
char ReadBuffer[ARRAYSIZE + 1];   // Read data buffer
char ErrorMnemonic[21][5] = {"EDVR", "ECIC", "ENOL", "EADR", "EARG",
                             "ESAC", "EABO", "ENEB", "EDMA", "",
                             "EOIP", "ECAP", "EFSO", "", "EBUS",
                             "ESTB", "ESRQ", "", "", "", "ETAB"};


void GPIBCleanup(int Dev, char* ErrorMsg);


int _cdecl main(void)  {

/*
 *
 ============================================================================
 *
 * INITIALIZATION SECTION
 *
 *
 ============================================================================
 */

/*
 *  Assign a unique identifier to the device and store in the variable
 *  Dev.  If the ERR bit is set in ibsta, call GPIBCleanup with an
 *  error message. Otherwise, the device handle, Dev, is returned and
 *  is used in all subsequent calls to the device.
 */
#define BDINDEX                0      // Board Index
#define PRIMARY_ADDR_OF_DMM    16      // Primary address of device
#define NO_SECONDARY_ADDR      0      // Secondary address of device
#define TIMEOUT                T10s   // Timeout value = 10 seconds
#define EOTMODE                1      // Enable the END message
#define EOSMODE                0      // Disable the EOS mode

    Dev = ibdev (BDINDEX, PRIMARY_ADDR_OF_DMM, NO_SECONDARY_ADDR,
                 TIMEOUT, EOTMODE, EOSMODE);
```

```c
    if (ibsta & ERR)
    {
        GPIBCleanup(Dev, "Unable to open device");
        return 1;
    }

/*
 *  Clear the internal or device functions of the device.  If the error
 *  bit ERR is set in ibsta, call GPIBCleanup with an error message.
 */

    ibclr (Dev);
    if (ibsta & ERR)
    {
        GPIBCleanup(Dev, "Unable to clear device");
        return 1;
    }

/*
 *
 * ========================================================================
 *
 *  MAIN BODY SECTION
 *
 *  In this application, the Main Body communicates with the instrument
 *  by writing a command to it and reading its response. This would be
 *  the right place to put other instrument communication.
 *
 *
 * ========================================================================
 */

/*
 *  Request the identification code by sending the instruction '*IDN?'.
 *  If the error bit ERR is set in ibsta, call GPIBCleanup with an error
 *  message.
 */

      ibwrt (Dev, "MARKMINI;OUTPACTI", 17L);
    if (ibsta & ERR)
    {
        GPIBCleanup(Dev, "Unable to write to device");
        return 1;
    }

/*
 *  Read the identification code by calling ibrd. If the ERR bit is
 *  set in ibsta, call GPIBCleanup with an error message.
 */

    ibrd (Dev, ReadBuffer, ARRAYSIZE);
    if (ibsta & ERR)
    {
        GPIBCleanup(Dev, "Unable to read data from device");
        return 1;
```

```
    }

/*
 *  Assume that the returned string contains ASCII data. NULL terminate
 *  the string using the value in ibcntl which is the number of bytes
 *  read in. Use printf to display the string.
 */
/* time example */


    ReadBuffer[ibcntl] = '\0';
    printf("Returned string:  %s\n", ReadBuffer);

      //Create a file to write to
    FILE *OutFile = fopen("S21freq.txt","a");
    //Send data to file
    fprintf(OutFile,"%s\n",ReadBuffer);
    //Close the file
    fclose(OutFile);

ibwrt (Dev, "OUTPMARK;MARKMINI", 17L);
    if (ibsta & ERR)
    {
        GPIBCleanup(Dev, "Unable to write to device");
        return 1;
    }

/*
 *  Read the identification code by calling ibrd. If the ERR bit is
 *  set in ibsta, call GPIBCleanup with an error message.
 */

    ibrd (Dev, ReadBuffer, ARRAYSIZE);
    if (ibsta & ERR)
    {
        GPIBCleanup(Dev, "Unable to read data from device");
        return 1;
    }

/*
 *  Assume that the returned string contains ASCII data. NULL terminate
 *  the string using the value in ibcntl which is the number of bytes
 *  read in. Use printf to display the string.
 */

    ReadBuffer[ibcntl] = '\0';
    printf("Returned string:  %s\n", ReadBuffer);

      //Create a file to write to
    FILE *OutFile1 = fopen("S11intensity.txt","a");
    //Send data to file
    fprintf(OutFile1,"%s\n",ReadBuffer);
    //Close the file
    fclose(OutFile1);


/*
```

```
 *
 =======================================================================
 *
 * CLEANUP SECTION
 *
 *
 =======================================================================
 */

/*  Take the device offline.
*/

    ibonl (Dev, 0);

    return 0;

}


/*
 *  After each GPIB call, the application checks whether the call
 *  succeeded. If an NI-488.2 call fails, the GPIB driver sets the
 *  corresponding bit in the global status variable. If the call
 *  failed, this procedure prints an error message, takes the
 *  device offline and exits.
 */
void GPIBCleanup(int ud, char* ErrorMsg)
{
    printf("Error : %s\nibsta = 0x%x iberr = %d (%s)\n",
            ErrorMsg, ibsta, iberr, ErrorMnemonic[iberr]);
    if (ud != -1)
    {
      printf("Cleanup: Taking device offline\n");
      ibonl (ud, 0);
    }
}
```

Network analyzer data save program (S$_{21}$)

```c
/*
 *  Include the WINDOWS.H and DECL-32.H files. The standard Windows
 *  header file, WINDOWS.H, contains definitions used by DECL-32.H and
 *  DECL-32.H contains prototypes for the GPIB routines and constants.
 */

#include "stdafx.h"
#include <stdio.h>
#include <time.h>

#define ARRAYSIZE 100              // Size of read buffer

int  Dev;                          // Device handle
char ReadBuffer[ARRAYSIZE + 1];    // Read data buffer
char ErrorMnemonic[21][5] = {"EDVR", "ECIC", "ENOL", "EADR", "EARG",
                             "ESAC", "EABO", "ENEB", "EDMA", "",
                             "EOIP", "ECAP", "EFSO", "", "EBUS",
                             "ESTB", "ESRQ", "", "", "", "ETAB"};


void GPIBCleanup(int Dev, char* ErrorMsg);


int _cdecl main(void)  {

/*
 *
 ========================================================================
 *
 * INITIALIZATION SECTION
 *
 *
 ========================================================================
 */

/*
 *  Assign a unique identifier to the device and store in the variable
 *  Dev.  If the ERR bit is set in ibsta, call GPIBCleanup with an
 *  error message. Otherwise, the device handle, Dev, is returned and
 *  is used in all subsequent calls to the device.
 */
#define BDINDEX                0     // Board Index
#define PRIMARY_ADDR_OF_DMM    16    // Primary address of device
#define NO_SECONDARY_ADDR      0     // Secondary address of device
#define TIMEOUT                T10s  // Timeout value = 10 seconds
#define EOTMODE                1     // Enable the END message
#define EOSMODE                0     // Disable the EOS mode

    Dev = ibdev (BDINDEX, PRIMARY_ADDR_OF_DMM, NO_SECONDARY_ADDR,
                 TIMEOUT, EOTMODE, EOSMODE);
    if (ibsta & ERR)
    {
        GPIBCleanup(Dev, "Unable to open device");
```

```c
        return 1;
    }

/*
 * Clear the internal or device functions of the device.  If the error
 * bit ERR is set in ibsta, call GPIBCleanup with an error message.
 */

    ibclr (Dev);
    if (ibsta & ERR)
    {
        GPIBCleanup(Dev, "Unable to clear device");
        return 1;
    }

/*
 *
 *========================================================================
 *
 *  MAIN BODY SECTION
 *
 *  In this application, the Main Body communicates with the instrument
 *  by writing a command to it and reading its response. This would be
 *  the right place to put other instrument communication.
 *
 *
 *========================================================================
 */

/*
 * Request the identification code by sending the instruction '*IDN?'.
 * If the error bit ERR is set in ibsta, call GPIBCleanup with an error
 * message.
 */



    ibwrt (Dev, "MARKMAXI;OUTPACTI", 17L);
    if (ibsta & ERR)
    {
        GPIBCleanup(Dev, "Unable to write to device");
        return 1;
    }

/*
 * Read the identification code by calling ibrd. If the ERR bit is
 * set in ibsta, call GPIBCleanup with an error message.
 */

    ibrd (Dev, ReadBuffer, ARRAYSIZE);
    if (ibsta & ERR)
    {
        GPIBCleanup(Dev, "Unable to read data from device");
        return 1;
    }

/*
```

```
 *  Assume that the returned string contains ASCII data. NULL terminate
 *  the string using the value in ibcntl which is the number of bytes
 *  read in. Use printf to display the string.
 */
/* time example */


    ReadBuffer[ibcntl] = '\0';
    printf("Returned string:  %s\n", ReadBuffer);

       //Create a file to write to
    FILE *OutFile = fopen("S21freq.txt","a");
    //Send data to file
    fprintf(OutFile,"%s\n",ReadBuffer);
    //Close the file
    fclose(OutFile);

ibwrt (Dev, "OUTPMARK;MARKMAXI", 17L);
    if (ibsta & ERR)
    {
       GPIBCleanup(Dev, "Unable to write to device");
       return 1;
    }

/*
 *  Read the identification code by calling ibrd. If the ERR bit is
 *  set in ibsta, call GPIBCleanup with an error message.
 */

    ibrd (Dev, ReadBuffer, ARRAYSIZE);
    if (ibsta & ERR)
    {
       GPIBCleanup(Dev, "Unable to read data from device");
       return 1;
    }

/*
 *  Assume that the returned string contains ASCII data. NULL terminate
 *  the string using the value in ibcntl which is the number of bytes
 *  read in. Use printf to display the string.
 */

    ReadBuffer[ibcntl] = '\0';
    printf("Returned string:  %s\n", ReadBuffer);

       //Create a file to write to
    FILE *OutFile1 = fopen("S21intensity.txt","a");
    //Send data to file
    fprintf(OutFile1,"%s\n",ReadBuffer);
    //Close the file
    fclose(OutFile1);


/*
 *
 ========================================================================
 *
```

```
 * CLEANUP SECTION
 *
 *
 ======================================================================
 */

/*  Take the device offline.
*/

    ibonl (Dev, 0);

    return 0;

}


/*
 *  After each GPIB call, the application checks whether the call
 *  succeeded. If an NI-488.2 call fails, the GPIB driver sets the
 *  corresponding bit in the global status variable. If the call
 *  failed, this procedure prints an error message, takes the
 *  device offline and exits.
 */
void GPIBCleanup(int ud, char* ErrorMsg)
{
    printf("Error : %s\nibsta = 0x%x iberr = %d (%s)\n",
            ErrorMsg, ibsta, iberr, ErrorMnemonic[iberr]);
    if (ud != -1)
    {
       printf("Cleanup: Taking device offline\n");
       ibonl (ud, 0);
    }
}
```

References

[1] J. W. Costerton, Philip S. Stewart, E. P. Greenberg, "Bacterial Biofilms: A Common Cause of Persistent Infections", SCIENCE, VOL 284, pp. 1318-1322, 21 May 1999

[2] D. G. Davies, A. M. Chakrabarty, G. G. Geesey, Appl. Environ. Microbiol. 59, 1181, 1993

[3] Sutherland, I. W. "Bacterial exopolysaccharides – their nature and production", Surface Carbohydrates of the Prokaryotic Cell, London, academic, pp. 27-96, 1977

[4] J. W. Costerton, Z. Lewandowski, D.E Caldwell, D.R. Corber, H.M. Lappin-Scott, Annu. Rev. Microbiol, 41, 435, 1987

[5] A. E. Khoury, K. Lam, B. D. Ellis, J. W. Costerton, Am. Soc. Artif. Intern. Organs J. 38, 174 (1992)

[6] Garth D. Ehrlich, Fen Ze Hu, Qiao Lin, J. William Costerton, and J. Christopher Post, "Intelligent Implants to battle Biofilms", ASM News, Volume 70, pp. 127-133, November 3, 2004

[7] Rabin O. Darouiche, "Treatment of infection Associated with Surgical Implants", N. Engl. J. Med., 350;14, pp.1422-1429, April 2004

[8] Thien-Fah C. Mah and George A. O'Toole, "Mechanisms of biofilm resistance to antimicrobial agents", TRENDS in Microbiology, Vol.9, No.1, pp34-39, January 2001

[9] E. Leoni, P.P. Legnani, Comparison of selective procedures for isolation and enumeration of Legionella species from hot water systems, J. Appl. Microbiol. 90 (2001) 27–33

[10] A.K. Bej, M.H. Mahbubani, J.L. Dicesare, R.M. Atlas, Polymerase chain reactiongene probe detection of microorganisms by using filter-concentrated samples, Appl. Environ. Microbiol. 57 (1991) 3529–3534.

[11] M.H. Mahbubani, A.K. Bej, R. Miller, L. Haff, J. DiCesare, R.M. Atlas, Detection of Legionella with polymerase chain reaction and gene probe methods, Mol. Cell. Probes 4 (1990) 175–187.

[12] Matthew D. Disney, Juan Zheng, Timothy M. Swager, Pter H. Seeberger, "Detection bacteria with coarbohydrate-functionalized fluorescent polyers", J. AM. CHEM. SOC, Vol.126, No. 41, pp 13343-13346, 2004

[13] E. Heyduk, T. Heyduk, "Fluorescent homogeneous immunosensors for detecting pathogenic bacteria", Anal. Biochem. 396, pp. 298-303, 2010

[14] Steven A. Soper et. al., "Pont of care biosensor systems for cancer diagnostics/prognostics", Biosensors and Bioelectronics, 21, pp.1932-1942, 2006

[15] Biosource invitrogen cytokines & Signaling, www.invitrogen.com

[16] Kalimuthu P, Tkac J, Kappler U, Davis JJ, Bernhardt PV, "Highly Sensitive and Stable Electrochemical Sulfite Biosensor Incorporating a Bacterial Sulfite Dehydrogenase", Analytical Chemistry, Volume 82, Issue 17, pp. 7374-7379, Sep 1 2010

[17] M.A. Alonso-Lomillo, O. Dominguez-Renedo, M.J. Arcos-Martinez, "Screen-printed biosensors in microbiology; a review", Talanta, 82, pp.1629-1636, 2010

[18] Joon Myong Song, Mustafa Culha, Paul M. Kasili, Guy D. Griffin, Tuan Vo-Dinh, "A compact CMOS biochip immunosensor towards the detection of a single bacteria", Biosensors and Bioelectronics 20, pp. 2203-2209, 2005

[19] L. Yang et al, "Interdigitated microelectrode (IME) impedance sensor for the detection of viable Salmonella typhimurium", Biosensors and Bioelectronics, 19, pp 1139-1147, 2004

[20] Peng Cong, Wen H. Ko, and Darrin J. Young, "Wireless Batteryless Implantable Blood Pressure Monitoring Microsystem for Small Laboratory Animals", IEEE SENSORS JOURNAL, VOL. 10, NO.2, pp.243-254, Feb. 2010

[21] Kerstin Lange, Bastian E. Rapp, and Michael Rapp, "Surface Acoustic Wave Biosensors: a review", Anal Bioanal Chem, 391, pp1509-1519, 2008

[22] Keekeun Lee, Wen Wang, Taehyun Kim, and Sangsik Yang, "A novel 440 MHz wireless SAW microsensor integrated with pressure-temperature sensors and ID tag", J. Micromech. Microeng, 17, pp515-523, 2007

[23] Biljana A. Cavic, Gordon L. Hayward, and Michael Thompson, "Acoustic Waves and the study of biochemical macromolecules and cells at the sensor-liquid interface", Analystm 124, pp. 1405-1420, 1999

[24] Soumya Krishnamoorthy, Agis A. Iliadis, "Properties of high sensitivity ZnO surface acoustic wave sensors on SiO_2/(100) Si substrates", Solid-State Electron., 52, pp. 1710-1716, 2008

[25] A. Springer, R. Weigel, A. Pohl, F. Seifert, "Wireless identification and sensing using surface acoustic wave devices", IEEE ASME Trans Mechatron, 9, pp. 745-756, 1999

[26] J-M Friedt, C. Droit, G. Martin, and S. Ballandras, "A wireless interrogation system exploiting narrowband acoustic resonator for remote physical quantity measurement", Review of Scientific Instruments, 81, 014701-014709, 2010

[27] Peter A. Lieberzeit, Christian Palfinger, Franz L. Dickert, and Gerhard Fischerauer, "SAW RFID-Tags for Mass-Sensitive Detection of Humidity and Vapors", Sensors, 9, pp 9805-9815, 2009

[28] Bill Drafts, "Acoustic Wave Technology Sensors", IEEE T MICROW THEORY, Vol. 49, No. 4, pp. 795-802, April 2001

[29] J. Du, G.L. Harding, J.A. Ogilvy, P.R. Dencher, M. Lake, "A study of Love-wave acoustic sensors", SENSOR ACTUAT A, 56, pp. 211-215, 1996

[30] K. Kalantar-Zdeh, D. A. Powell, "Comparison of layered based SAW sensors", SENSOR ACTUAT B-CHEM, 91, pp.303-308, 2003

[31] Re-Ching Lin, Ying-Chung Chen, Wei –Tsai Chang, Chien-chuan Cheng, Kuo-Sheng Kao, "Highly sensitive mass sensor using film bulk acoustic resonator", SENSOR ACTUAT A, 147, pp. 425-429, 2008

[32] Kourosh Kalantar-Zadeh, David A. Powell, Wojtek Wlodarski, Samuel Ippolito, Kosmas Galatsis, "Comparison of layered based SAW sensors", SENSOR ACTUAT B, 91, pp. 303-308, 2003

[33] G. McHale, M. I. Newton, and F. Martin, "Theoretical mass sensitivity of Love wave and layer guided acoustic plate mode sensors", J. APPL PHYS, Vol. 91, No. 12, pp. 9701- 9710, 15 June 2002

[34] Glen McHale, "Generalized concept of shear horizontal acoustic plate mode and Love wave sensors", Meas. Sci. Technol., 14, pp.1847-1853, 2003

[35] Chengtao Yang, Jiahe Dong, Heping Xie, Jianxiong Li, and Shuren Zhang, "Calculation of the dispersion properties of Rayleigh wave on ZnO/Metal/Diamond/Si-layered structure", INTEGR FERROELECTR, 84, pp. 39-48, 2006

[36] I.D. Avramov, A. Voigt and M. Rapp, "Rayleih SAW resonators using gold electrode structure for gas sensor applications in chemically reactive environments", Electronics Letters, 31st, Vol. 41, No.7, March 31st 2005

[37] http://en.wikipedia.org/wiki/Rayleigh_wave

[38] Nachappa Gopalsami, Ivan Osorio, Stanislav Kulikov, Sergey Buyko, Andrey Martynov, and ApostolosC. Raptis, "SAW Microsensor Brain Implant for prediction and Monitoring of Seizures", IEEE SENSORS JOURNAL, VOL. 7, NO.7, pp.977-982, July 2007

[39] Mattews H., Van de Vaart, "Observation of Love Wave Propagation at UHF Frequencies", Applied Physics Lettersm Volume 14, Issue 5, pp. 171-172, Mar 1969

[40] Sean Wu, Zhi-Xun Lin, Ruyen Ro, and Maw-Shung Lee, "Rayleigh and Shear Horizontal Surface Acoustic Properties of (100) ZnO Films on Silicon", IEEE T ULTRASON FERR, Vol.57, No.5, May 2010

[41] Glen McHale, "Generalized concept of shear horizontal acoustic plate mode and Love wave sensors", Meas. Sci. Technol., 14, pp. 1847-1853, 2003

[42] E. Gizeli, N.J. Goddard, C.R. Lowe and A.C. Stevenson, "A Love plate biosensor utilizing a polymer layer", SENSOR ACTUAT B-CHEM, 6 (1992), pp. 131-137

[43] G. Kovacs, G.W. Lubking, M.J. Vellekoo, and A. Vennema, "A Love wave sensor for (bio) chemical sening in liquids", SENSOR ACTUAT A, 43 (1994), pp. 38 – 43

[44] Soumya Krishnamoorthy, Agis A. Iliadis, Thaleia Bei, George P. Chrousos, "An interleukin-6 ZnO/SiO2/Si surface acoustic wave biosensor", Biosensors and Bioelectronics, 24, pp. 313-318, 2008

[45] D.D. Stubbs, L.Sang-Hun and W.D. Hunt, "Molecular recognition for electronic noses using surface acoustic wave immunoassay sensors", *IEEE sensors*, vol. 2, no. 2, pp. 294-300, 2002.

[46] Heh-Nan Lin, Sy-hann chen, Shu-Te ho and Ping-Ren Chen, I-Nan Lin, "Comparative measurements of the piezoelectric coefficient of a lead zirconate titanate film by piezoresponse force microscopy using electrically characterized tips", J. Vac. Sci. Technol. B 21(2), pp 916-918, Mar/Apr 2003

[47] M.C. Horrillo, M.J. Fernandez, J.L. Fontecha, I. Sayago, "Optimization of SAW sensors with a structure ZnO-SiO2-Si to detect volatile organic compounds", SENSOR ACTUAT B, 118 (2006), pp.356-361

[48] Y.Q. Fu et. al. "Recent developments on ZnO films for acoustic wave based bio-sensing and microfluidic applications: a review", SENSOR ACTUAT B, 143, pp. 606-619, 2010

[49] Zhou Li, Rusen Yang, Min Yu, Fan Bai, Cheng Li, and Zhong Lin Wang, "Cellular Level Biocompatibility and Biosafety of ZnO Nanowires", Journal of Physical Chemistry C Letters, 112, pp.20114-20117, 2008

[50] A Szczepanik et al. "ZnO nanostructures by Atomic Layer Deposition Method", Journal of Physics, conference Series 146, 012017, 2009

[51] Lamia Znaidi, "Sol-gel-deposited ZnO thin films: A review", Material Science and Engineering:B, Volume 174, Issue 1-3, pp.18-30, 25 Oct 2010

[52] Pappas David L. et al., "Pulsed laser deposition of diamond-like carbon films", Journal of Applied Physics, Volume 71, Issue 11, pp. 5675-5684, 1992

[53] Chang-Feng Yu, Sy-Hann Chen, Shih-Jye Sun, and Chou, "Influence of the substrate temperature on the electrical and magnetic properties of ZnO: N thin films grown by pulse laser deposition", Journal of PhysicsD: Applied Physics, 42, 035001, 2009

[54] Soumya Krishnamoorthy, and Agis A. Iliadis, "Development of ZnO/SiO2/Si Love Mode Surface Acoustic Wave Devices with High Sensitivity for Biosensor Applications", IEEE Sensors Applications Symposium, Houston, Texas, USA, 7-9 Feb 2006

[55] Wu Ping, Cheng Jingzhi, "Theory of acoustic impedance matching of ultrasonic transducers", Proceedings of the Annual International Conference of the IEEE, Vol.3, pp 1281, 4-7 Nov 1988

[56] Guigen Zhang, "Nanostructure-Enhanced surface acoustic waves biosensor and its computational modeling", journal of Sensors, Volume 2009, Article ID 215085, 2009

[57] Zerrouki C et al, "Shear Horizontal Surface Acoustic Waves Sensor for Label-Free DNA Detection", Sensor Letters, Volume 8, Issue 6, pp.813-817, Dec 2010

[58] Chengtao Yang, Jiahe dong, Heping Xie, Jianxiong Li, and Shuren Zhang, "Calculation of the Dispersion Properties of Rayleigh Wave on ZnO/Metal/Diamond/Si-Layered Structure", Integrated Ferroelectrics, 84, pp. 39-48, 2006

[59] X.Y. Du et al, "ZnO film for application in surface acoustic wave device", Journal of Physics: Conference Series 76, 012035, 2007

[60] Axelevitch A, Gorenstein B, Darawshe H, Golan G, "Investigation of thin solid ZnO films preparaed by sputtering", THIN SOLID FILMS, Volume 518, Issue 16, pp.4520-4524, June 1 2010

[61] Y.W. Kim, S. E. Sardari, A.A. Iliadis, and R. Ghodssi, "A Bacterial Biofilm Surface Acoustic Wave Sensor for Real Time Bacterial Growth Monitoring", IEEE Sensors 2010, November1-4, Hawaii, pp1568-1571

[62] F. Herrmann, D. Hahn, S. Buttgenbach, „Separation of density and viscosity influence on liquid-loaded surface acoustic wave devices", Applied Physics Letters, Volume 74, Number 22, pp. 3410-3412, May 31st 1999

[63] NIST Property Data Summaries, http://www.ceramics.nist.gov/srd/summary/emodox00.htm

[64] http://www.lenntech.com/teflon.htm, http://www.cctplastics.com/teflonall.html

[65] Hang Ju Ko et. al., „Improvement of the quality of ZnO substrates by annealing", Journal of Crystal Growth, 269, pp.493-498, 2004

[66] http://cp.literature.agilent.com/litweb/pdf/5965-7707E.pdf

[67] Wen-Ching Shih, Tzyy-Long Wang, and Yi-Ling Kuo, "Accelerating Effect of Aluminum Oxide Films on surface Acoustic Wave on Crystalline Quartz", Jappanese Journal of Applied Physics, 48, 07GG11, 2009

[68] Lynda Charters, "Aluminum Oxide orbital implant has better biocompatibility", Ophthalmology Times, June 15, 2001

[69] Wang NF, Tsai YZ, Tang T, Houng MP, "S-Band Low-loss wide bandwidth microwave surface acoustic wave filter", Microwave Journal, Volume 52, Issue 9, pp.144-158, Sep 2009

[70] G. Mchale, M. I. Newton, and F. Martin, "theoretical mass sensitivity of Love wave and layer guided acoustic plate mode sensors", J. of App. Phys., Volume 91, Number 12, pp. 9701-9710, 2002

[71] V. Raimbault, D. Rebiere, and C. Dejous, "A microfluidic surface acoustic wave sensor platform: Application to high viscosity measurements", Material Science and Engineering C, 28, pp.759-764, 2008

[72] M.H. Zwietering et al.,"Modeling of the Bacterial Growth Curve", Applied and Environmental Microbiology, pp. 1875-1881, June 1990

[73] Jeffrey V. Straight and Doraiswami Ramkrishna, "Modeling of Bacterial Growth under Multiply-Limiting Conditions. Experiments under Carbon- or/and Nitrogen-Limiting Conditions", Biotechnol. Prog. 10, pp.588-605, 1994

[74] Freudenberg J, Schelle S, Beck K, Von Schickfus M, Hunklinger S, "A contactless surface acoustic wave biosensor", Biosensors & Bioelectronics, Volume 14, Issue 4, pp.423-425, APR 30 1999

[75] SAI LIU et al, "Detection of Explosive Vapors by Surface Acoustic Wave Sensors Containing Novel Siloxane Based Coatings", Journal of Macromolecular Science, Part A, Pure and Applied Chemistry, 47, pp.1172-1175, 2010

[76] Xiaoying Zhu, Renbi Bai, Kin-Ho Wee, Changkun Liu, Shu-Ling Tang, "Membrane surfaces immobilized with ionic or reduced silver and their anti-biofouling performances", Journal of Membrane Science, 363, pp278-286, 2010

[77] Rodnwy Komlenic, "Rethinking the causes of membrane biofouling", Filtration & Separation, Volume 47, Issue 5, pp. 26-28, Sep-Oct 2010

[78] Kogai T, Yoshimura N, Mori T, Yatsuda H, "Liquid-Phase Shear Horizontal Surface Acoustic Wave Immunosensor", Japanese Journal of Applied Physics, Volume 49, Issue 7, 07HD15, 2010

[79] Wegmueller MS, Kuhn A, Froehlich J, Oberie M, Felber N, "An attempt to model the human body as a communication channel", IEEE Transactions on Biomedical Engineering, Volume 54, Issue 10, pp.1851-1857, OCT 2007